JOURNAL OF AIRCRAFT
Vol. 51, No. 6, November–December 2014

Real-Time Flight Simulation of Highly Maneuverable Unmanned Aerial Vehicles

Michael S. Selig*
University of Illinois at Urbana–Champaign, Urbana, Illinois 61801

DOI: 10.2514/1.C032370

This paper focuses on full six degree-of-freedom aerodynamic modeling of small unmanned aerial vehicles at high angles of attack and high sideslip in maneuvers performed using large control surfaces at large deflections for aircraft with high thrust-to-weight ratios. Configurations, such as this, include many of the currently available propeller-driven radio-controlled model airplanes that have control surfaces as large as 50% chord, deflections as high as 50 deg, and thrust-to-weight ratios near 2:1. Airplanes with these capabilities are extremely maneuverable and aerobatic, and modeling their aerodynamic behavior requires new thinking because using traditional stability-derivative methods is not practical with highly nonlinear aerodynamic behavior and coupling in the presence of high prop-wash effects. The method described outlines a component-based approach capable of modeling these extremely maneuverable small unmanned aerial vehicles in a full six degree-of-freedom real-time environment over the full ±180 deg range in angle of attack and sideslip. Piloted flight-simulation results for four radio-controlled/unmanned-aerial-vehicle configurations having wingspans in the range from 826 mm (32.5 in.) to 2540 mm (100 in.) are presented to highlight the results of the high-angle aerodynamic modeling approach. Maneuvers simulated include tailslides, knife-edge flight, high-angle upright and inverted flight, rolling maneuvers at high angle, and an inverted spin of a biplane. For each case, the flight trajectory is presented together with time histories of aircraft-state data during the maneuvers, which are discussed.

Nomenclature

A	=	propeller-disc area
a	=	airfoil lift-curve slope, 2π
b	=	wingspan
C_d	=	drag coefficient
C_l	=	lift coefficient
$C_{m,c/4}$	=	moment coefficient about quarter chord
C_Q	=	propeller torque coefficient, $Q/\rho n^2 D^5$
C_T	=	propeller thrust coefficient, $T/\rho n^2 D^4$
c	=	mean aerodynamic chord, camber
D	=	drag, propeller diameter
J	=	propeller advance ratio based on V_N
L	=	lift
M	=	pitching moment about y axis, positive nose up
N_P	=	propeller yawing moment due to angle of attack
n	=	propeller rotational speed, rev/s
P_N	=	propeller normal force due to angle of attack
p, q, r	=	roll, pitch, and yaw rates
$\bar{p}, \bar{q}, \bar{r}$	=	nondimensional roll, pitch, and yaw rates; $pb/2V$, $qc/2V$, $rb/2V$
Q	=	propeller axial torque
q	=	dynamic pressure, $\rho V^2/2$
R	=	propeller radius
S	=	reference area
T	=	propeller axial thrust
u, v, w	=	components of the local relative flow velocity along x, y, z, respectively
V	=	flow velocity
x, y, z	=	body-axis coordinates, $+x$ out nose, $+y$ out right wing, $+z$ down
y_c	=	airfoil camber

Symbols

α	=	angle of attack, $\arctan(w/u)$
β	=	sideslip angle, $\arcsin(v/V)$
β'	=	angle of attack for vertical surface, $\arctan(v/u)$
δ_a	=	aileron deflection $[(\delta_{a,r} - \delta_{a,l})/2]$, right positive trailing-edge up, left positive trailing-edge up
δ_e	=	elevator deflection, positive trailing-edge down
δ_r	=	rudder deflection, positive trailing-edge left
ϵ	=	wing induced angle of attack
η_s	=	dynamic pressure ratio for flow-shadow (shielding) effect
ρ	=	air density
σ	=	propeller solidity, blade area/disc area
ϕ, θ, ψ	=	bank angle, pitch angle, heading angle

Subscripts

N	=	normal component
R	=	relative component

Superscript

$\bar{(\ )}$	=	normalized quantity, average quantity

I. Introduction

THERE is a growing interest in modeling and understanding full-envelope aircraft flight dynamics, that is, modeling the aircraft over the full ±180 deg range in angle of attack and sideslip. Flight outside the normal envelope like this can be encountered in airplane stall/spin situations, or more generally upset scenarios that can be caused by a host of factors (e.g., pilot, aircraft, and weather). Moreover, aerobatic airplanes routinely enter and exit controlled flight outside the envelope with precision and grace. Interest in full-envelope aircraft flight dynamics has also been fueled in recent years by the rapid growth in unmanned aerial vehicles (UAVs) (both civilian and military), together with synergistic parallel advances in high-performance radio-controlled (RC) model aircraft.

Presented as Paper 2010-7635 at the AIAA Atmospheric Flight Mechanics 2010 Conference, Toronto, ON, Canada, 2–5 August 2010; received 4 April 2013; revision received 7 March 2014; accepted for publication 12 March 2014; published online 3 November 2014.

*Associate Professor, Department of Aerospace Engineering, 104 South Wright Street. Associate Fellow AIAA.

Within the broad spectrum of UAV/RC configurations has emerged a general category that is capable of extremely agile maneuvers, such as vertical and/or short take-off and landing-like flight; hovering; perching; stop and stare; defensive and evasive postures; and rapid roll, pitch, yaw rates and accelerations [1–7]. The high agility derives from having control surfaces as large as 50% chord with deflections as high as ± 50 deg and propeller thrust-to-weight ratios of near 2:1. A tractor-propeller-driven fixed-wing RC variant that falls in this category is shown in Fig. 1, with the large control surfaces at neutral, and then deflected to illustrate their full extent.

These configurations clearly present new challenges to flight dynamics simulation and modeling because of the combined considerations of high-angle full-envelope flight, large highly deflected control surfaces, strong propeller-wash effects, high thrust, and concomitant unsteady flow. In the general case, modeling aircraft over the full envelope is not likely to be successful using a stability-derivative approach because of the strong nonlinearities and coupling effects. Physical wind-tunnel measurements also fall short of capturing the aerodynamics of the full static and dynamic envelope due to a number of factors; for example, the sheer time and expense of a full test campaign, as well as the most basic issue of wind-tunnel wall effects, such as propeller-wash recirculation within the test section, present many challenges [8]. However, recent measurements presented in [9] are a notable exception, wherein a full aerobatic vehicle configuration was tested in a vertical wind tunnel. One might envision using brute-force computational fluid dynamics (CFD) analyses to generate lookup-table data for a full vehicle, but the computational resources needed to cover a typical flight envelope in a reasonable period of time exceed current-day capabilities [10–12]. Although modeling agile static and dynamic flight presents a plethora of challenges for CFD techniques, some new approaches might make it more feasible to consider in the future [13]. Aircraft system identification (ID) methods [14,15], as with all of the aforementioned techniques, could be used to provide insight in special cases, but the general application of system ID methods to full-envelope aerodynamic modeling would be daunting.

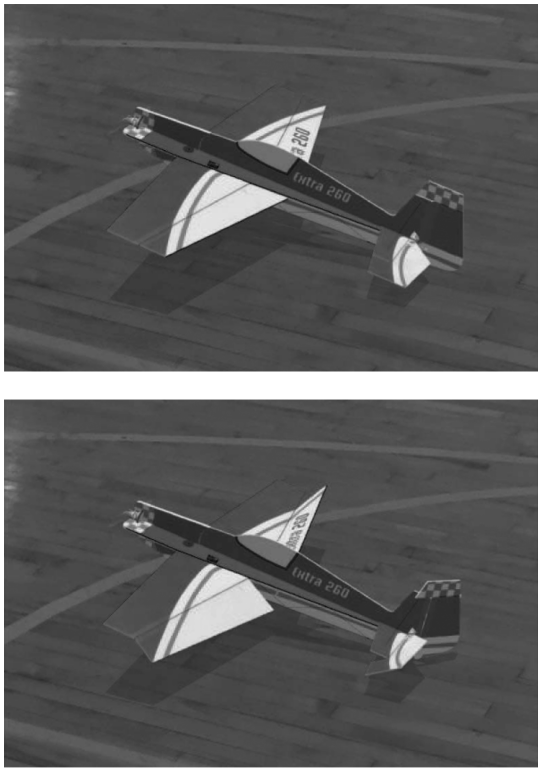

Fig. 1 Extra 260 EFL aerobatic foam-construction electric propeller-driven RC aircraft with large control surfaces at neutral and maximum deflections [wingspan of 826 mm (32.5 in.)].

With the primary objective of this research being full-envelope 6-degree-of-freedom (DOF) simulation of agile aircraft in low subsonic flight, a feasible approach after considering some of the alternatives is to use a component-buildup methodology that relies as much as possible on first-principles aerodynamic modeling supported by lookup tables for any data that can be obtained a priori (e.g., aerodynamic coefficient data covering the full ± 180 deg range). As with any component-buildup approach, the evaluation of the component forces and moments can rely on data from myriad sources (e.g., wind-tunnel measurements; analytical predictions; CFD results [16]; empirical/semi-empirical methods; and data compendia, such as the U.S. Air Force Data Compendium [17] and ESDU data [18]). The superposition of all elements of the model, taking into account any appropriate interaction effects, then yields the summation of all forces and moments acting on the total vehicle airframe. This general approach has been applied to a wide range of problems in modeling and simulation, for example, propeller-dominated UAV flight dynamics [5,6,19]; ducted-fan configurations [20]; autonomous underwater vehicles [21]; wing-only tumbling analysis [22]; high-angle-of-attack longitudinal aircraft trim analysis [23]; and poststall flight dynamics, spin, and upset modeling [24–30], to name a few.

As described in this paper, a component-buildup method was developed for UAV/RC aircraft. In particular, the full-envelope aerodynamic modeling framework described here is that which is implemented in real time in the FS One® RC flight simulator [31]. This paper focuses on the methods used in modeling the wing, fuselage, and tail surfaces of a conventional, yet highly maneuverable, aerobatic configurations. Propeller effects are included in the method and discussed, but a more in-depth description of the propeller aerodynamic modeling is included in [32]. Example maneuvers predicted by the method are illustrated and discussed. It is worth adding that, while components can be added to the method, they can also be removed, and as such, easily and realistically simulate damaged aircraft or faulty system components [33].

II. Model Requirements

In this research, the requirements from the outset were to create a real-time simulation environment capable of modeling the flight dynamics of small, agile UAV/RC configurations. As stated, these vehicles have high thrust-to-weight ratios near 2:1 and use large control surfaces at high deflections immersed in strong propeller wash. Consequently, the trimmable flight envelope is large, and the range of dynamic maneuvers is spectacular.

The trimmable flight envelope to be captured in simulation includes all of the nominal trimmed states (e.g., straight flight and turning flight). While normal cruise flight is the nominal condition, these highly maneuverable UAV/RC aircraft can fly outside the envelope in trim at high angles of attack near 45 deg with nose-up elevator input — the so-called harrier maneuver in RC parlance. This flight condition relies on lift from the wing and also the vertical component of thrust to sustain level trimmed flight. Taken further with more nose-up elevator and additional thrust, the flight can be arrested to a 90 deg angle-of-attack stationary-hovering attitude that uses only thrust to support the aircraft weight. This hover condition can also be entered from steady knife-edge flight that is extended with large rudder input to an extreme 90 deg yaw that again ends in a stationary-hovering attitude. All of these conditions were required to be captured in the simulation.

Apart from trimmed flight, other dynamic maneuvers to be captured by the simulation are much more complex. These include the classic stall from upright longitudinal flight and also wingtip stall that can precipitate into a fully developed spin. The spin can be characterized by a number of descriptors, for example, it can be an upright spin or inverted spin with either a nose-down attitude or flat spin with power added or not, all resulting in extremely complex aerodynamic states to model. "Blender" is the particular name given to inverted power-on flat spins that are dramatic, and this same maneuver can be entered and momentarily sustained from a level high-speed flight condition. Snaps, tailslides, hammerheads, and

knife-edge stall are also dynamic maneuvers that are aerobatic in nature and lead to high-angle flight conditions. Modern RC models with high thrust capabilities can also perform what are called rolling harriers, which are a high pitch angle, slow, rolling maneuver that requires modulating elevator and rudder input (out of phase) to keep a nose-high attitude while simultaneously rolling with near-constant aileron input. These rolling harriers can be flown in straight flight, turning flight, loops or horizontal (or vertical) figure eights, etc. Apart from upset conditions that are accidentally encountered, these maneuvers clearly depend on varying degrees of pilot skill to perform. Simulating these maneuvers poses unique and formidable challenges in aerodynamic modeling.

Finally, the simulation framework (including graphics, physics, pilot inputs, recording features, and more) was required to run in real time on a high-performance desktop PC. Clearly, this computational environment sets additional requirements on the aerodynamic modeling methodology to make it robust and also capable of simulating nominal, agile, and aerobatic flight over a range of situations. The remainder of this paper henceforth will focus on the aerodynamic modeling and simulation that achieve all of the broad requirements that have been outlined in this section.

III. Technical-Development Process

The development began with a relatively simple approach — that of using stability derivatives. However, during the core development period (3 years), each element of the stability-derivative approach was replaced by methods that could capture the full envelope with enough generality to simulate flight in any attitude.

Out of this fundamental bottom-up approach arose the capability to simulate highly nonlinear complex maneuvers that are observed in actual flight across a spectrum of aircraft. In fact, the framework was applied equally across an array of more than 30 aircraft covering myriad configurations that ranged from simple rudder–elevator glider trainers to ones having propulsion (jet and propeller) with large flaps, ailerons, elevator, and airbrakes [31]. The technical development also directly benefited from physical measurements, flight video, and feedback from professional RC pilots and aircraft designers.

IV. Component Aerodynamic Models

In the model, the aircraft is divided into basic components, such as the wing, horizontal tail, vertical tail, propeller, etc., and for each, a separate model is developed to determine the contribution that each component makes to the total forces and moments on the aircraft at each point in time. For each component, the local relative flow is determined, taking into account aircraft speed and rotations (assuming rigid-body kinematics), together with wind, turbulence, and any aerodynamic interference effects, such as propeller wash, wing induced flow, shielding effects (e.g., tail blanketing in spin), ground effect, and more. For most of the models, the component state (relative flow, surface deflections, and other data as it might apply) is then used to determine any related aerodynamic coefficient data. The final component dynamic pressure, aerodynamic coefficient data, and respective reference area are then used to determine the forces and moments. This basic approach applies to the simplest component models, while in most cases, additional steps are taken or an entirely different approach is used involving analytical and/or empirical/semi-empirical methods built upon some physical basis. Finally, in the method, quasi-steady aerodynamic methods are applied, and dynamic stall is not modeled.

A. Wing Aerodynamics

The wing aerodynamics produce the most dominant forces and moments, and thus, careful modeling is key to simulating full vehicle performance. Challenges in predicting this performance include mainly high-angle (±180 deg) performance and large control surfaces at high deflections. Other important elements include wing-in-propeller slipstream effects, induced flow produced by the wing, shielding of one wing on another (biplane wings), apparent mass, and flow-curvature effects. In most cases, the reduced frequency in pitch is small enough that dynamic stall effects are small, and thus, this effect is not currently included in the model.

To run in real time, there must be a balance between using on-the-fly fundamental physics methods and precomputed data that can be accessed quickly through lookup tables. For the wing, these precomputed data include the full aerodynamic coefficients (C_l, C_d, $C_{m,c/4}$) and induced angle of attack as a function of any control-surface deflections. These data are local values at stations along the wing, that is, the wing is discretized, and in the simulation, a strip-theory approach is applied, as will be described.

As a method, strip theory is used for aircraft aeroelastic simulations [34], and routinely for blade-element theory in the rotorcraft field [35]. Strip-theory approaches have also been applied to wings in a trailing vortex flow and aircraft spin prediction (e.g., [30,36–39] and others cited therein). It seems that only recently has the general strip-theory approach been applied in real-time simulation for fixed-wing force and moment calculations [6,28,29]. (In this work, the strip-theory approach was used from the outset beginning in 2003. It should be mentioned that a strip-theory approach is used in the X-Plane™ commercial flight simulator as briefly mentioned online by the company [40].)

Various approaches to implementing a strip-theory approach have been applied for fixed-wing and rotary-wing aircraft. In this work, the approach is to use a nonlinear lifting-line code to determine the local induced angle of attack at each section along the wing over a range of angles of attack and control-surface deflections. Thus, lookup tables are created for the local two-dimensional (2-D) induced angle ϵ as a function of the local 2-D angle of attack α and local control-surface deflection. In the method, the local three-dimensional (3-D) flow for an element of the wing is composed of the sum of all velocity components due to aircraft motion, propeller wash, and wind, along with corrections for any shielding that might be modeled on the element. From this direct flow calculation, the local 2-D angle of attack is obtained and used to find the induced angle through lookup tables. A ground-effect correction is also applied when in ground proximity. Taking all these contributions into account, the angle of attack of the relative flow becomes

$$\alpha = \alpha_{\text{direct flow}} + \epsilon + \Delta\alpha_{\text{ground effect}} \tag{1}$$

Figure 2 shows this angle of attack for an element of the wing along with the local normal flow component V_N corresponding to the local relative flow V_R. Using the angle of attack, the corresponding section lift, drag, and moment coefficients are found through lookup tables, and if the section operates in the poststall regime, some corrections

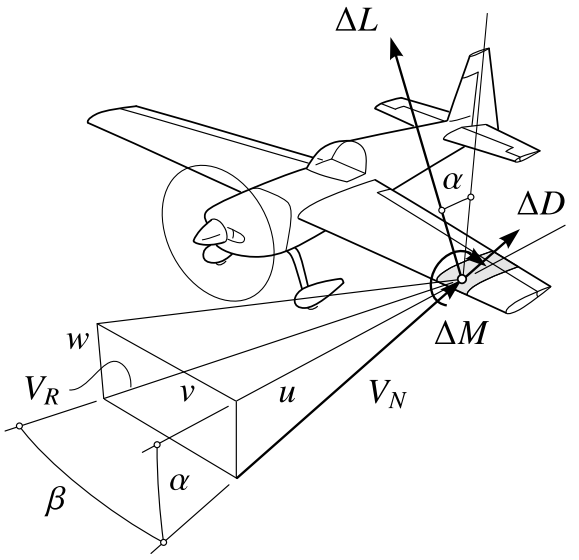

Fig. 2 Convention showing local flow for a strip of the wing and resulting in-plane lift, drag, and moment (Edge 540 aircraft configuration).

are applied. The resulting lift, drag, and moment at the quarter-chord location of the element are given by

$$\Delta L = q_N \Delta S C_l \tag{2}$$

$$\Delta D = q_N \Delta S C_d \tag{3}$$

$$\Delta M = q_N \Delta S c C_{m,c/4} \tag{4}$$

in which

$$q_N = q_R \cos^2 \beta \tag{5}$$

The resulting location of the element is then used to transfer these data to the aircraft center of gravity.

The approach relies on a number of lookup tables that are interpolated in real time. For a typical wing, 20 elements may be used along the wing, with some elements naturally aligned on the edges of control surfaces, at dihedral breaks, or positioned inside the propeller wash. Each element includes its associated tables for the airfoil lift, drag, and moment coefficients, as well as the local induced angle of attack. Other tables are included to account for any propeller wash and shielding that may exist, depending on the position of the element along the wing. Thus, at a minimum, a typical wing during real-time execution will use 80 tables of data and more if additional effects are included. For a biplane, the number of tables for the wing system doubles. Also, as it relates to biplane wings, consistent with the strip-theory approach and given the typical spacing between the upper and lower biplane wings, the section properties are based on 2-D airfoil characteristics, with the upper and lower wing airfoils considered in isolation.

The ShowTime 50 aircraft shown in Fig. 3 is representative of some popular RC aerobatic configurations with large control surfaces that can be deflected to high angles. The aircraft is produced and distributed by Hangar 9™, and a scaled-down variant has been examined recently in experiments designed to study wing rock [41]. As seen in Fig. 3, the 1.45 m (57 in.) wingspan aircraft has wing side-force generators (SFGs) (which are optional) for greater performance in knife-edge flight. The particular control-surface sizes for the ShowTime 50 are shown in Fig. 4 for the inboard aileron, elevator, and rudder for deflections of 15, 30, and 50 deg.

The aerodynamic performance characteristics for these high deflections for the full range cannot yet be reliably predicted using CFD; however, there are a number of numerical and experimental sources of data that can be used as guides in generating the necessary data over the full angle-of-attack range of ± 180 deg. For the wing airfoil, the data-fusion process combines any available experimental data with predictions from XFOIL [42] for low angles of attack and small flap deflections, and for high flap deflections and high angles of attack (including reverse flow beyond ± 90 deg [43]), a flat-plate-theory [44] approach is employed to yield results like those shown in Fig. 5. These particular results are for the ShowTime 50 inboard-wing airfoil, but many of the trends in the poststall region (where the flat-plate theory applies, e.g., [44]) are similar across a range of airfoils, with differences depending largely on airfoil thickness, camber, control-surface size, and leading-edge radius. Figures 6 and 7 present the lift- and drag-coefficient data as the lift-to-drag (C_l/C_d) ratio and in airfoil polar (C_l vs C_d) format, respectively. These are convenient ways of viewing and interpreting the data, and it makes for easy comparison across a range of literature (airfoil data for aircraft, sailing, motorsports, and wind energy). Because the wing airfoil shown in Fig. 4 is symmetrical, the data shown in Figs. 5–7 reflect this fact. It should be mentioned that the aerodynamic coefficient data presented in this paper correspond to the Reynolds number for nominal cruise flight for the respective aircraft, and no interpolation on Reynolds number was performed. This approach is appropriate because most of the simulation results (later in Sec. V) are for a high-angle-of-attack flight, in which there is separated flow, and thereby,

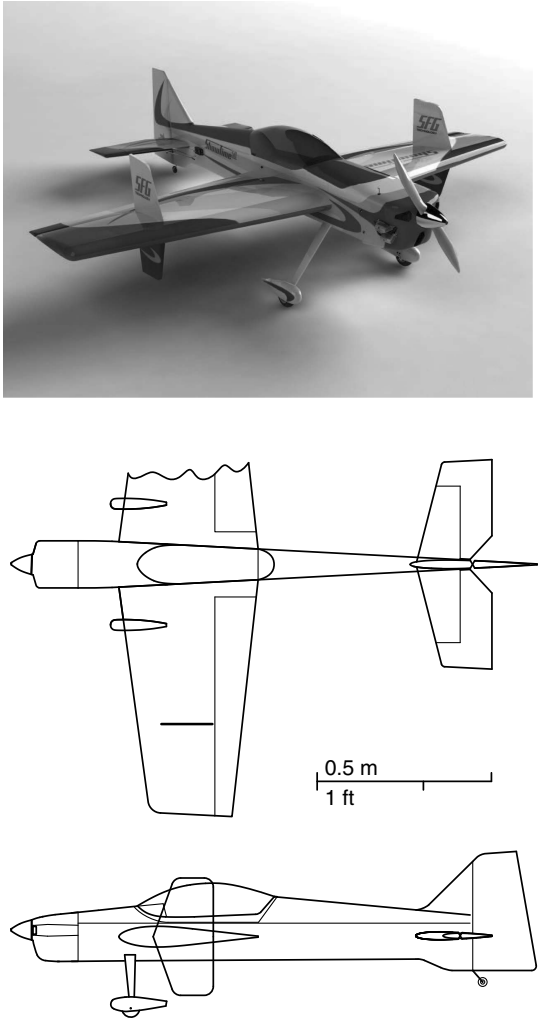

Fig. 3 ShowTime 50 aerobatic RC aircraft configured with elevator, rudder, ailerons, and wing dual SFGs.

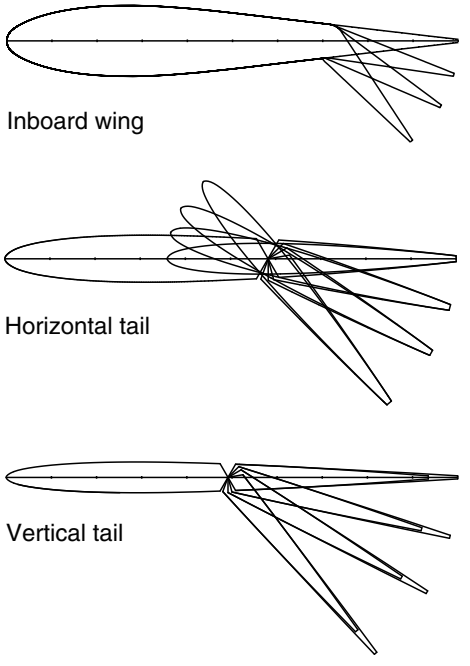

Fig. 4 Airfoil sections used on the ShowTime 50 with control-surface deflections of 15, 30, and 50 deg.

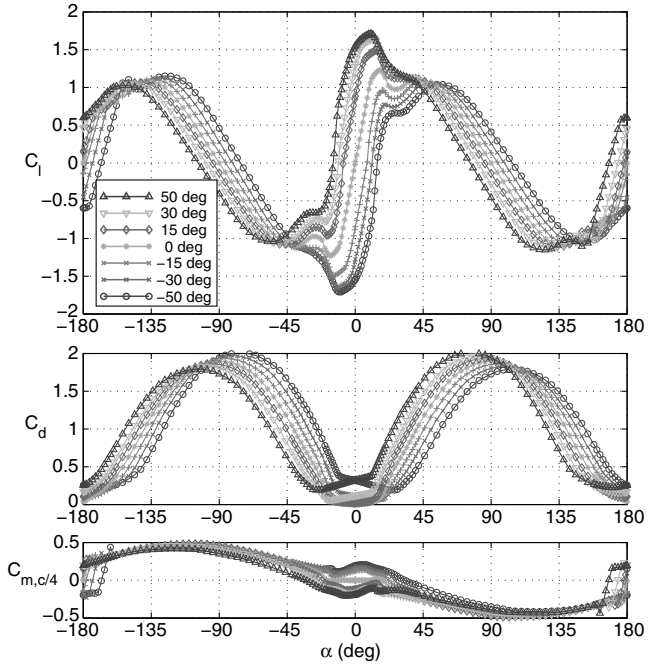

Fig. 5 Airfoil performance over the full ±180 deg angle-of-attack range for aileron deflections of 0, ±15, ±30, and ±50 deg.

Reynolds-number effects are not dominant for the aircraft sizes considered. Also, during a real-time simulation, linear interpolation is used to obtain the aerodynamic coefficients as functions of the angle of attack and control-surface deflection.

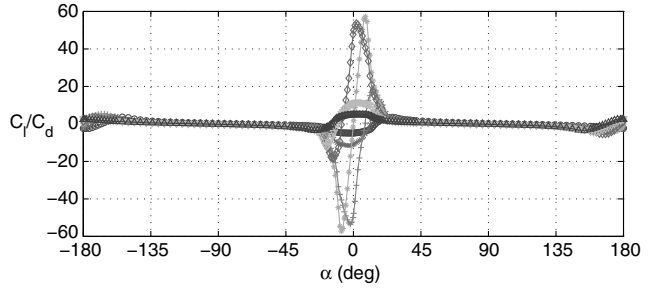

Fig. 6 Airfoil lift-to-drag characteristics over the full ±180 deg angle-of-attack range for aileron deflections of 0, ±15, ±30, and ±50 deg (see Fig. 5 for legend).

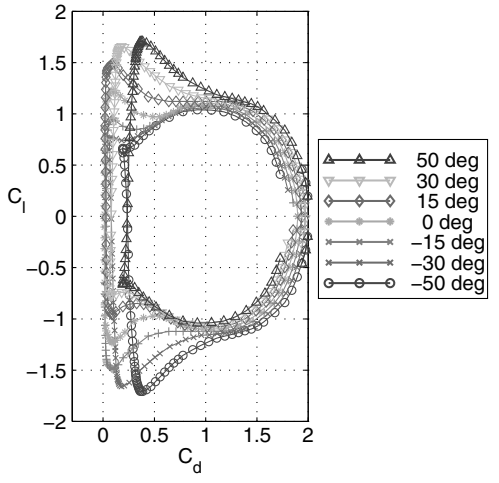

Fig. 7 Airfoil polar over the ±90 deg angle-of-attack range for aileron deflections of 0, ±15, ±30, and ±50 deg.

From the known wing geometry and airfoil data as shown, a nonlinear lifting-line code was written to determine the local induced angle of attack for a given wing angle of attack and control-surface deflection. The procedure starts with an estimated circulation distribution $\hat{\Gamma}_i$ concentrated on the quarter-chord line along the wing. From this estimate, the downwash distribution $\hat{w}_i$ is obtained using the Biot–Savart law, and this is used to determine the local lift coefficient $\hat{C}_l$ using lookup tables based on data like that shown in Fig. 5. With this lift coefficient and the local geometric properties, a new estimate for the circulation $\hat{\Gamma}_{\text{new}}$ is determined. If this new estimate matches the initial values within a small, specified tolerance, the solution has converged; otherwise, the iteration continues with underrelaxation being used to obtain a new estimate for the circulation determined by

$$\hat{\Gamma}_{i+1} = \omega\hat{\Gamma}_{\text{new}} + (1-\omega)\hat{\Gamma}_i \tag{6}$$

This process is repeated for a 2-D sweep over the control-surface deflections and angle of attack (nominally $-20 \text{ deg} < \alpha < 20 \text{ deg}$), and the data are saved as a lookup table. During a real-time simulation, the induced angle of attack is tapered to zero at the limits at an absolute angle of attack of 90 deg. Thus, beyond ±90 deg, the induced angle of attack is assumed to be zero, which is reasonable, considering that, at 90 deg, the wing lift is nearly zero, and beyond this point, the aircraft remains in this state (in reverse flow) only momentarily, while most likely undergoing large angle-of-attack excursions (e.g., in a tailslide maneuver).

The lifting-line approach was applied to both monowings and biplane wings. However, for biplane wings, an additional wash or interference effect must be taken into account. In a normal upright cruising flight, the bound vorticity on the lower wing produces a rearward wash on the upper wing, and the upper wing produces a forward wash on the lower wing. In general, this induced flow is determined during a real-time simulation by computing the net strength of the bound vorticity for each wing, and then using the Biot–Savart law to compute the wash components, taking into account the effects of stagger for the upper and lower wings.

As seen in Fig. 5, around an angle of attack near 90 deg, the drag coefficient C_d is ≈2 and consistent with the flat-plate theory, with corrections that were developed for control-surface deflections. For a wing with a moderate aspect ratio, however, the drag coefficient C_D at 90 deg is lower than the 2-D case [45]; thus, an additional correction must be used to take this into account. For a flat-plate wing at an angle of attack of 90 deg, the pressure on the downstream leeward side is nearly constant because the separated flow cannot support a pressure gradient, and this result can be seen in pressure distributions of wind-turbine blades at 90 deg to the flow [46,47]. Consequently, the drag coefficient in the 90 deg case will be nearly constant along the entire wing, and CFD predictions for flat-plate wings are consistent with this fact [48]. Hence, beyond the stall angle of attack, that is, when the flow is separated, approximately constant pressure on the downstream side of the wing is established, and as complex as the flow may seem, a 2-D assumption, and hence, the strip-theory approach can still be used as a model of the flow. This observation was applied in creating the poststall 3-D corrections to the 2-D airfoil data.

Figure 8 shows the nonflapped airfoil data for the symmetrical ShowTime 50 airfoil shown in Fig. 5. Over the poststall range where the correction should be applied, the airfoil data are corrected for 3-D poststall effects as follows. For the 90 deg case alone, various empirical curve fits have been given for the wing drag coefficient $C_{D_{90}}$ as a function of the wing airfoil drag coefficient $C_{d_{90}}$ and wing aspect ratio AR [49]. In this development, it is necessary to form a correction that applies not just at 90 deg, but over the entire poststall range of angles of attack. The full-envelope 2-D to 3-D correction used here begins with a modification of the 90 deg case given by Lindenburg [50], namely

$$C_{d_{90}} = 2.2\{1 - 0.41[1 - \exp(-17/AR)]\} \tag{7}$$

in which, here, the wing aspect ratio AR is used instead of an effective aspect ratio AR_{eff} used by Lindenburg. This value $C_{d_{90}}$ is simply normalized to provide the scaling factor used in the next step, that is

$$k_{C_d} = C_{d_{90}}/2.2 \tag{8}$$

The final drag used for each element of the wing is then given by

$$C_{d,\text{corrected}} = C_d[1 - w(1 - k_{C_d})] \tag{9}$$

in which w is a cosine weighting function expressed as

$$w = \cos\left[\pi\left(\frac{\alpha - \alpha_{P,1}}{\alpha_{N,2} - \alpha_{P,1}}\right) - \frac{\pi}{2}\right] \tag{10}$$

in which $\alpha_{P,1}$ and $\alpha_{N,2}$ define the range over which the correction applies, tapering to zero at the ends. Furthermore, to maintain the necessary poststall relationship that $C_L/C_D \approx 1/\tan\alpha$ [51], the same correction is applied to the local lift coefficient, namely

$$C_{l,\text{corrected}} = C_l[1 - w(1 - k_{C_d})] \tag{11}$$

Moreover, because the moment in the poststall region is driven largely by the drag acting on the 50% chord location (the center of pressure), the correction also applies to the moment coefficient, namely

$$C_{m,c/4,\text{corrected}} = C_{m,c/4}[1 - w(1 - k_{C_d})] \tag{12}$$

Figure 8 shows the application of this approach over the range of 0–180 deg for the inboard-wing airfoil lift- and drag-coefficient data for the zero-aileron-deflection case that was previously presented in Fig. 5. The original airfoil data are shown together with the corrected data and the cosine weighting function applied over the range −25 to 160 deg, which approximately defines the poststall region for this airfoil. More sophisticated approaches [52] could be used for blending in the corrections via the weighting function, Eq. (10), but the current approach closely models experimental data and has the benefit of being computationally efficient for use in a real-time simulation.

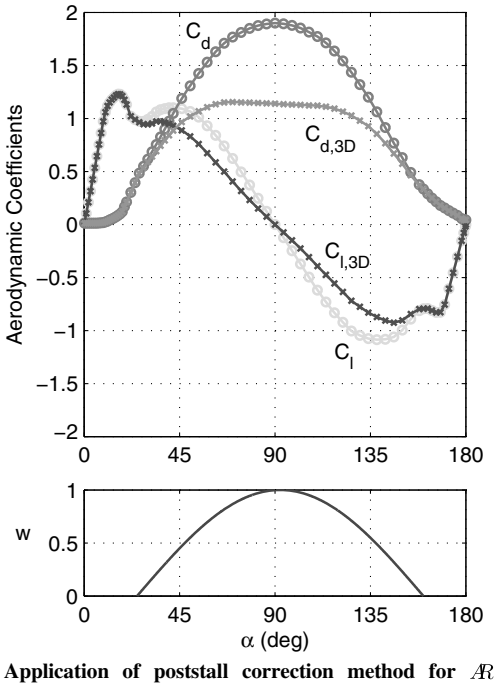

Fig. 8 Application of poststall correction method for $AR = 4.5$ showing the uncorrected airfoil data, corrected airfoil data (3-D), and weighting function w used in the correction for the angle-of-attack range of 0–180 deg.

Another important effect that is modeled includes effective camber produced by pitch rate [53,54]. A positive pitch rate increases the lift coefficient and moment. Only the pitch-rate effect on lift is discussed here. The effective circular-arc camber produced by a pitch rate about an axis located at the midchord is illustrated in Fig. 9. As shown, the pitch rate induces a flow perpendicular to the airfoil, which, in this diagram, is represented as a flat plate (Fig. 9a). As shown in Fig. 9b, when the freestream is added to this pitch-rate component, the local flow to the chord line is angled. Solving for the flow is equivalent to that of a cambered airfoil with zero pitch rate, as shown in Fig. 9c, in which the local angle to the chord line is equivalent to that in Fig. 9b. The slope of the effective camberline in Fig. 9c is given by

$$\frac{\mathrm{d}y}{\mathrm{d}x} = \frac{w}{V} = \frac{\dot{\alpha}}{Vc}\left(\frac{x}{c} - \frac{1}{2}\right) \tag{13}$$

which, upon integration to obtain the effective camberline, yields

$$\frac{y}{c} = \frac{\dot{\alpha}}{2Vc}\frac{x}{c}\left(\frac{x}{c} - 1\right) \tag{14}$$

The effective circular-arc camber produced by a pitch rate about an axis located at the midchord ($x/c = 1/2$) is then given by

$$(y_c/c)_{\text{eff}} = \frac{\dot{\alpha}}{8Vc} \tag{15}$$

The pitch-rate increment in the section lift coefficient is then obtained from

$$\Delta C_{l,\text{due to pitch rate}} = (y_c/c)_{\text{eff}}\frac{\partial C_l}{\partial(y_c/c)} \tag{16}$$

in which it is taken that $\partial C_l/\partial(y_c/c) \approx 12$, which is based on results from XFOIL [42], and approximates the camber effects of low-Reynolds-number airfoils. It should be noted, however, that this value does vary depending on the nominal Reynolds number and specific airfoil. By this method, the final section lift increment [Eq. (16)] is close to that obtained from quasi-steady thin-airfoil theory when the pitch occurs about the 50% station [54], in which case there is no additional pure angle-of-attack contribution. This latter additional contribution from thin-airfoil theory and the plunge effect is not included in this lift increment because these effects are already accounted for by using the relative-velocity approach for all components. The final lift increment derives from the wing lift coefficient for the ideal case given by

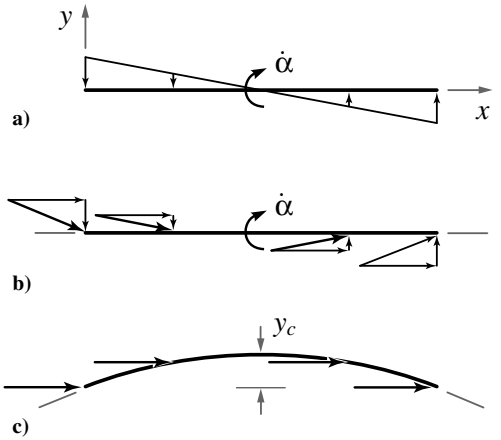

Fig. 9 Effective camber produced by the pitch rate: a) flow component due to rotation, b) total flow due to rotation plus freestream, and c) resulting effective camber without rotation in a freestream flow.

$$C_L = C_{l_\alpha}\left(\frac{AR}{AR+2}\right)\alpha \tag{17}$$

Taking the derivative of Eq. (17) with respect to the angle of attack can be used to obtain the effective camber wing lift increment as

$$\Delta C_{L,\text{due to pitch rate}} = \Delta C_{l,\text{due to pitch rate}}\left(\frac{AR}{AR+2}\right) \tag{18}$$

In a real-time simulation, to avoid any physically unrealizable ΔC_L values determined by this method (e.g., caused by a spike in $\dot{\alpha}$ produced by a rapid nose-up bounce upon landing), the computed increments are limited to a narrow range (e.g., $\Delta C_L \approx \pm 0.25$).

Finally, it is worth noting that, by using a strip-theory approach and taking into account the spanwise local relative flow, roll damping due to roll rate is captured intrinsically. For instance, in a roll, the downgoing wing experiences an increased angle of attack, and the upgoing wing a decrease, and consequently, the roll motion is damped. Similarly, the horizontal- and vertical-tail surfaces experience relative flow components due to pitch and yaw rates, thereby providing pitch and yaw damping, respectively.

B. Tail-Surface Aerodynamics

Unlike the wing, the tail surfaces are modeled as full surfaces without the use of strip theory. As with the wing, the aerodynamics of the tail surfaces are modeled over the full ±180 deg range in angle of attack and sideslip. As shown in Fig. 4, the flap sizes and maximum deflections can be extreme, and this requires relying partly on semi-empirical methods to capture the full-envelope performance. Wash models are also taken into account. First, the propeller wash on the tail surfaces is especially important because, in some conditions, the tail surfaces are completely immersed in the propeller wash (e.g., during hover on propeller thrust alone). Also, propeller slipstream flow curvature and propeller-wash lag are critically important aerodynamics to capture. Second, the wing downwash is taken into account, as well as the ground-effect aerodynamics through a downwash correction. Lag of wake downwash is not presently included. Of course, an effect that must be modeled is the shielding or blanketing that occurs around the tail surfaces, and in some situations, promotes and sustains aircraft spin. While all of these effects and others are modeled in the simulation, not all of these considerations are presented in this paper.

Typically, tail surfaces have relatively low aspect ratios, and much data on such wings exist in the literature, some including flaps and high-angle-of-attack data [54–66]. These references were used along

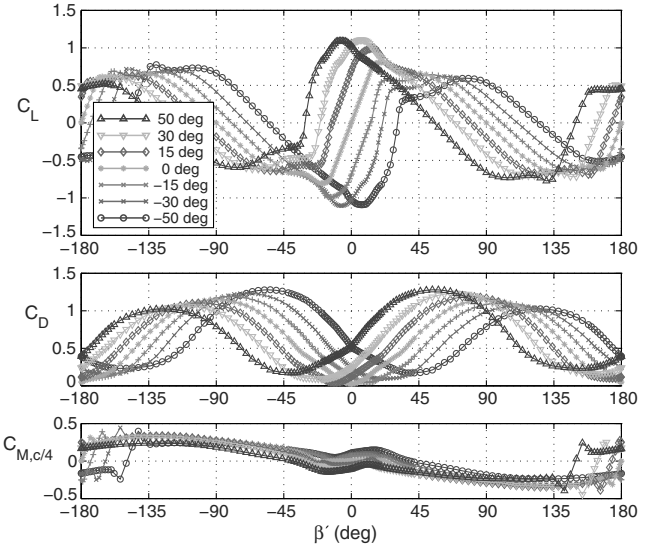

Fig. 10 Vertical-tail performance over the full ±180 deg side angle-of-attack range for rudder deflections of 0, ±15, ±30, and ±50 deg.

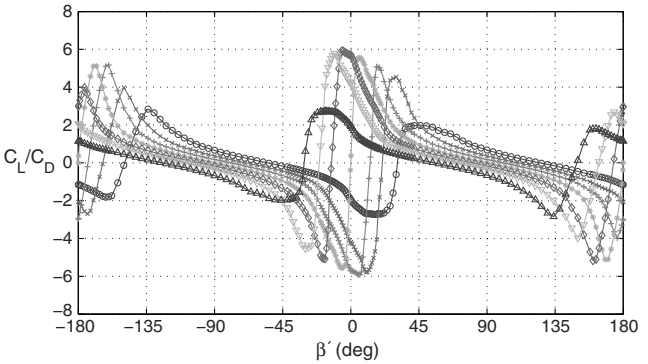

Fig. 11 Vertical-tail lift-to-drag characteristics over the full ±180 deg side angle-of-attack range for rudder deflections of 0, ±15, ±30, and ±50 deg (see Fig. 10 for legend).

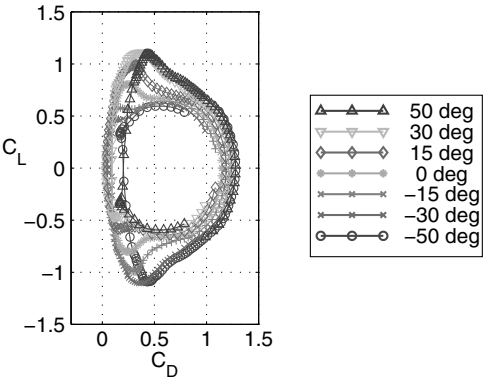

Fig. 12 Vertical-tail polar over the ±90 deg side angle-of-attack range for rudder deflections of 0, ±15, ±30, and ±50 deg.

with semi-empirical methods to construct full ±180 deg data. For the vertical fin of the ShowTime 50 model, the rudder control-surface ratio S_r/S is 0.68, which is extreme (see Fig. 3). Using the methods developed for modeling such surfaces, the data shown in Figs. 10–12 were generated. In this particular case, the data correspond to the part of the vertical fin above the horizontal tail, while the remainder of the vertical fin below the horizontal tail is modeled separately. In both cases, the horizontal tail acts as an end plate, and the lift-curve slopes are therefore increased using the method described in [23].

The propeller wash on the tail surface begins with the classic-momentum-theory result [67] that the flow through the propeller disc is given by

$$V_1 = V_\infty + w \tag{19}$$

in which

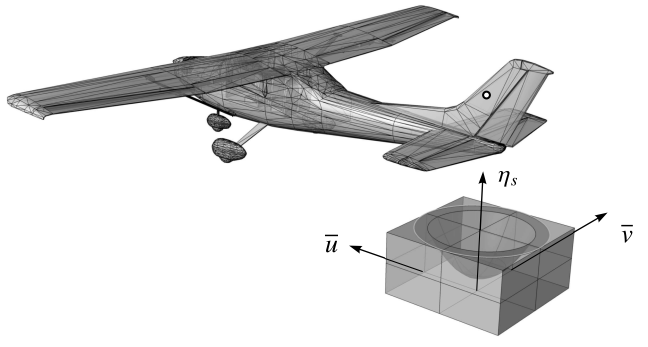

Fig. 13 Flow-shadow-map approach used in modeling the shielding effect of the horizontal tail on the vertical fin for flow coming from beneath.

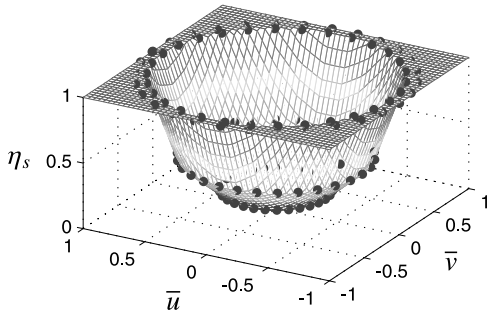

Fig. 14 Flow-shadow-map data used in modeling the shielding effect of the horizontal tail on the vertical fin for flow coming from beneath for the Cessna 182 RC model.

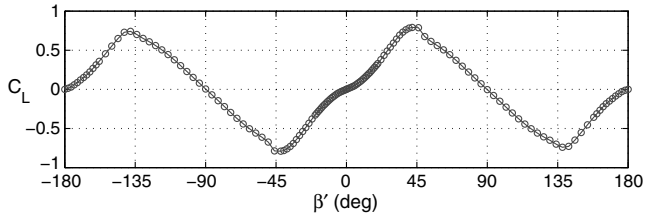

Fig. 15 Fuselage side-force lift coefficient over the full ±180 deg side angle-of-attack range.

$$w = \frac{1}{2}\left[-V_\infty + \sqrt{V_\infty^2 + \left(\frac{2T}{\rho A}\right)}\right] \tag{20}$$

There are a number of additional steps that are considered when extending this basic theory to flow at the tail in the general case of full-envelope flight, which can include flight in yawed flow, unsteady aircraft motions, wake-lag effects, and propeller hover and steep descent conditions. These propeller effects are discussed in [32].

Wing downwash on the horizontal tail is modeled in real time from the wing lift distribution and the geometry of the wing relative to the tail. From the lift distribution at any moment in time, the circulation distribution along the wing is determined. This vorticity is then shed into the wake as discrete filaments, that is, a system of horseshoe vortices that satisfy vortex continuity laws (Helmholtz theorem). The system includes vortices trailed from the wingtips and also inboard with alignment on aileron–flap junctures if they exist. Corrections are applied for wake contraction [68], angle of attack, sideslip, wall effect, and others. These wake characteristics are then used to determine the downwash at each tail surface.

The aerodynamics of the tail surfaces can be strongly influenced by the surrounding surfaces when operating in high-angle conditions. For instance, for a conventional tail-surface arrangement in a 90 deg plunge, the vertical fin will not be exposed to the total relative flow velocity because the flow will be masked, or shielded, by the horizontal-tail surface. In effect, the vertical fin, in this case, will be operating in the near-stagnant flow shadow of the horizontal tail. For this case described, the effect is most dramatic for the 90 deg plunge, but it attenuates to zero as the angle of attack is reduced back to nominal cruise flight conditions.

In spin, the same effect has been long recognized, and the discussion in McCormick [67] of a tail damping power factor that encapsulates the shielding effect dates back to research by the NACA in 1946 [69]. The method, developed as a design criterion for spin resistance, was later found to be not generally reliable [70], and in its formulation as a criterion, it was not suggested as a model of the flow for use in predicting aerodynamic forces. In [71], surface pressure on the vertical tail of a spin model was taken, and in [72], yaw-moment measurements in spin were obtained for a fuselage with various tail configurations, but deriving a shielding model from these data would be daunting. An elliptical bubble shielding model based on angle of attack was presented in [38], and it was applied to decrease the effective area of the vertical fin during spin. In the present work, a new 3-D model is described, and it is applied to estimate the flow speed and direction, not to decrement the area.

Figure 13 shows the approach used in modeling this tail-surface shielding effect. The vertical fin for this aircraft operates in the flow shadow of the horizontal tail for off-nominal high-angle conditions. A flow-shadow map is constructed to model the fraction η_s relating the local relative flow to the total relative flow, that is

$$\eta_s = \frac{V_{R,\text{local}}}{V_{R,\text{total}}} \tag{21}$$

in which $V_{R,\text{local}}$ is the flow exposed to the vertical fin, and $V_{R,\text{total}}$ is that determined from kinematics of the component. The fraction η_s ranges from zero (stagnant local flow) to 1 (no shielding present), and in this case, for flow from below, η_s is functionally defined here as

Table 1 Specifications for airplanes modeled (metric units)

Name	Category	b, m	S, dm^2	AR	l, m	W, g	W/S, g/dm^2
Edge 540	Aerobatic, scale, IMAC[a]/3-D, gas	2.48	111.68	5.492	2.16	10,205.83	90.30
Extra 260 EFL	Foamie, 3-D, ARF[b]	0.83	16.77	4.063	0.84	240.40	14.08
ShowTime 50	Aerobatic, 3-D, gas, ARF	1.45	46.58	4.500	1.51	2,902.99	61.54
ShowTime 50 SFG	Aerobatic, 3-D, gas, ARF	1.45	46.58	4.500	1.51	3,025.46	64.22
Ultimate TOC	Aerobatic, scale, IMAC/3-D	2.54	213.55	3.021	2.79	18,170.91	84.06

[a]International Miniature Aerobatic Club.
[b]Almost-Ready-To-Fly.

Table 2 Specifications for airplanes modeled (English units)

Name	Category	b, in.	S, in.^{2}	AR	l, in.	W, lb	W/S, oz/ft^2
Edge 540	Aerobatic, scale, IMAC/3-D, gas	97.50	1,731.00	5.492	85.00	22.50	29.95
Extra 260 EFL	Foamie, 3-D, ARF	32.50	260.00	4.063	33.00	0.53	4.67
ShowTime 50	Aerobatic, 3-D, gas, ARF	57.00	722.00	4.500	59.50	6.40	20.41
ShowTime 50 SFG	Aerobatic, 3-D, gas, ARF	57.00	722.00	4.500	59.50	6.67	21.30
Ultimate TOC	Aerobatic, scale, IMAC/3-D	100.00	3,310.00	3.021	110.00	40.06	27.88

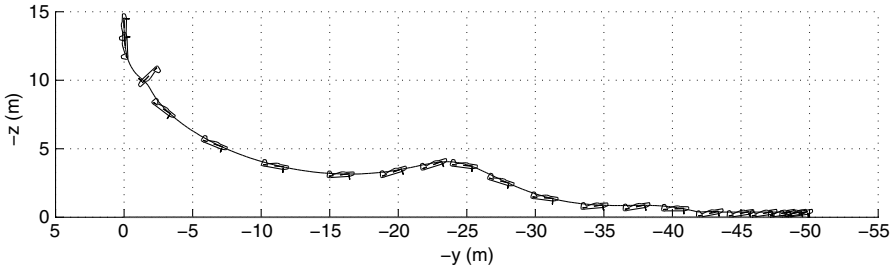

Fig. 16 Trajectory of the Extra 260 EFL aerobatic aircraft performing a tailslide [aircraft magnified 2.5 times the normal size and drawn every 0.55 s; wingspan of 826 mm (32.5 in.)].

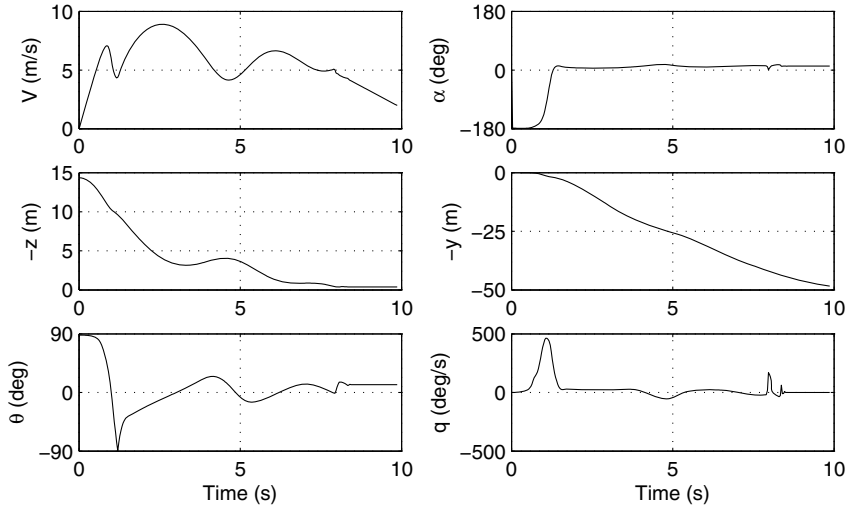

Fig. 17 Time history of the Extra 260 EFL aerobatic aircraft performing a tailslide (see Fig. 16 for trajectory).

$$\eta_s = f(\bar{u}, \bar{v}) \tag{22}$$

in which $\bar{u}$ and $\bar{v}$ are the direction cosines for the total relative flow vector on the surface. Figure 14 shows the flow-shadow map used to model this effect for the flow shadow on the vertical fin as a result of the horizontal tail beneath (case depicted in Fig. 13).

The flow-shadow maps are used extensively to model shielding effects. For instance, vertical fins that extend on either side of the horizontal tail (shown in Fig. 3) are modeled by using two flow-shadow maps — one as shown in Fig. 13 for the upper vertical fin and another for the lower vertical fin, in which flow from above is masked by the horizontal tail. Flow-shadow maps are also used on the horizontal-tail surfaces when flow is from the opposite side of the surface (captures shielding from the vertical fin and fuselage). Moreover, flow-shadow maps are used on the inboard sections of the wing for flow from either side at high sideslip. For biplanes, flow-shadow maps are used for each wing element to account for the shielding of one wing on the other. For aircraft with SFGs (see Fig. 3), flow maps are used much like that for the vertical fin with shielding from the horizontal tail. These maps, in general, are not axisymmetric, but instead, sometimes squashed on one side, depending on the local geometry that produces the shielding, or in some cases, these flow-shadow maps are 2-D instead of 3-D like Fig. 13. These maps are semi-empirical models, but like many semi-empirical models, these flow-shadow maps could ultimately be refined using experimental data or CFD.

C. Fuselage Aerodynamics

Fuselage aerodynamics are modeled by dividing the fuselage into segments and determining the local relative flow, which is then used together with the aerodynamic coefficients to yield the local forces, which, as in all cases, are then resolved about the center of gravity. Figure 15 shows the ShowTime 50 side-force lift coefficient for one panel (normalized by the panel area) for the full ±180 deg side

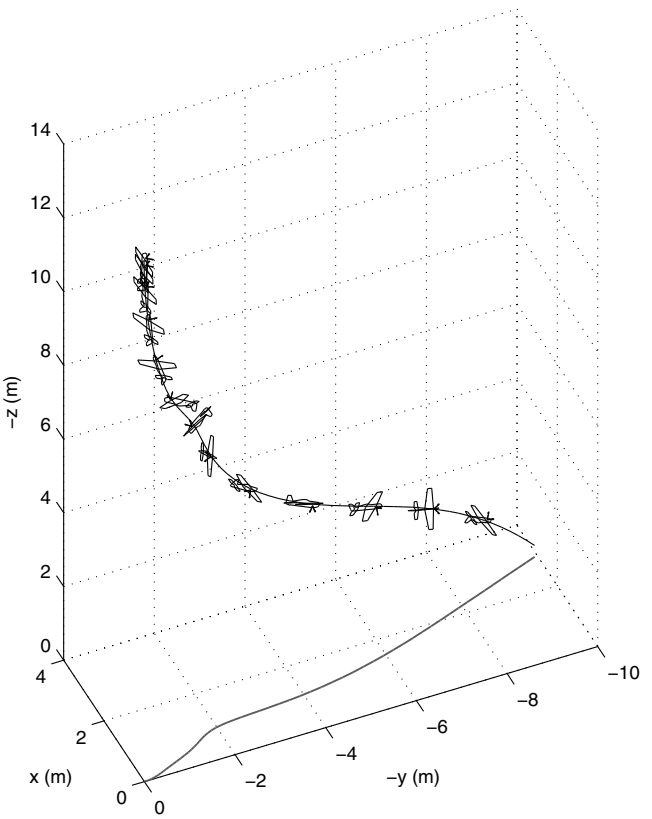

Fig. 18 Trajectory of the Extra 260 EFL aerobatic aircraft performing a tailslide with full left aileron input [aircraft normal size and drawn every 0.2 s; wingspan of 826 mm (32.5 in.)].

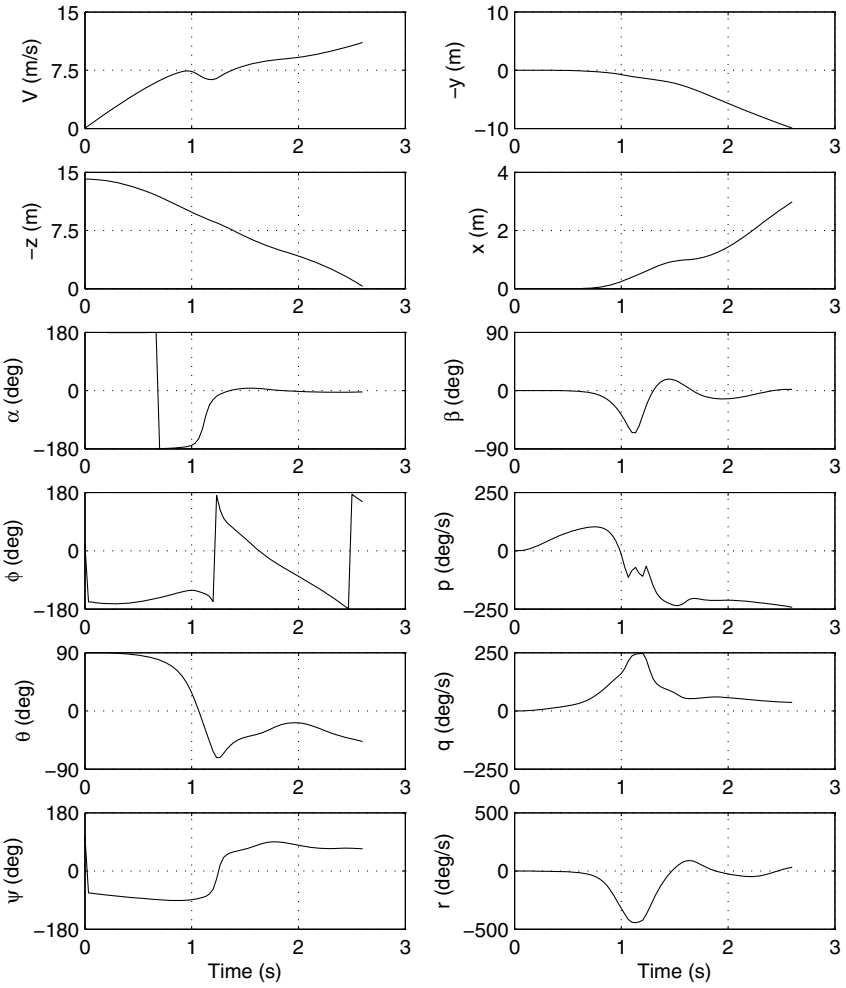

Fig. 19 Time history of the Extra 260 EFL aerobatic aircraft performing a tailslide with full left aileron input (see Fig. 18 for trajectory).

angle-of-attack β' range. The local flow is a summation of that from kinematics and wash models (propeller and downwash, including propeller-wash-lag effects). Elements of the development rely on methods that have been used in missile aerodynamics; however, again, no stability derivatives are applied.

D. Propeller Aerodynamics

Only a summary of the propeller force and moment modeling is included here, whereas details are given in [32]. For the normal working state (steady axial-flow conditions), the propeller thrust and torque are given by

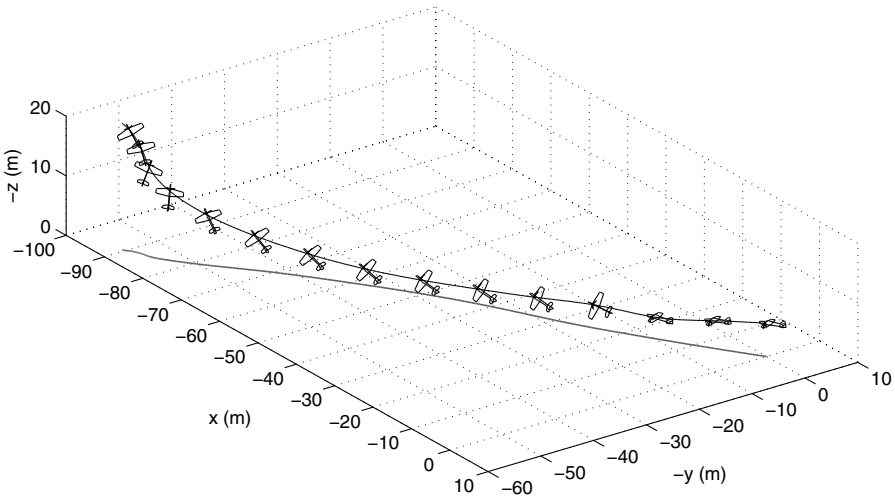

Fig. 20 Trajectory of the ShowTime 50 aerobatic aircraft in knife-edge flight [aircraft magnified three times the normal size and drawn every 0.5 s; wingspan of 1448 mm (57 in.)].

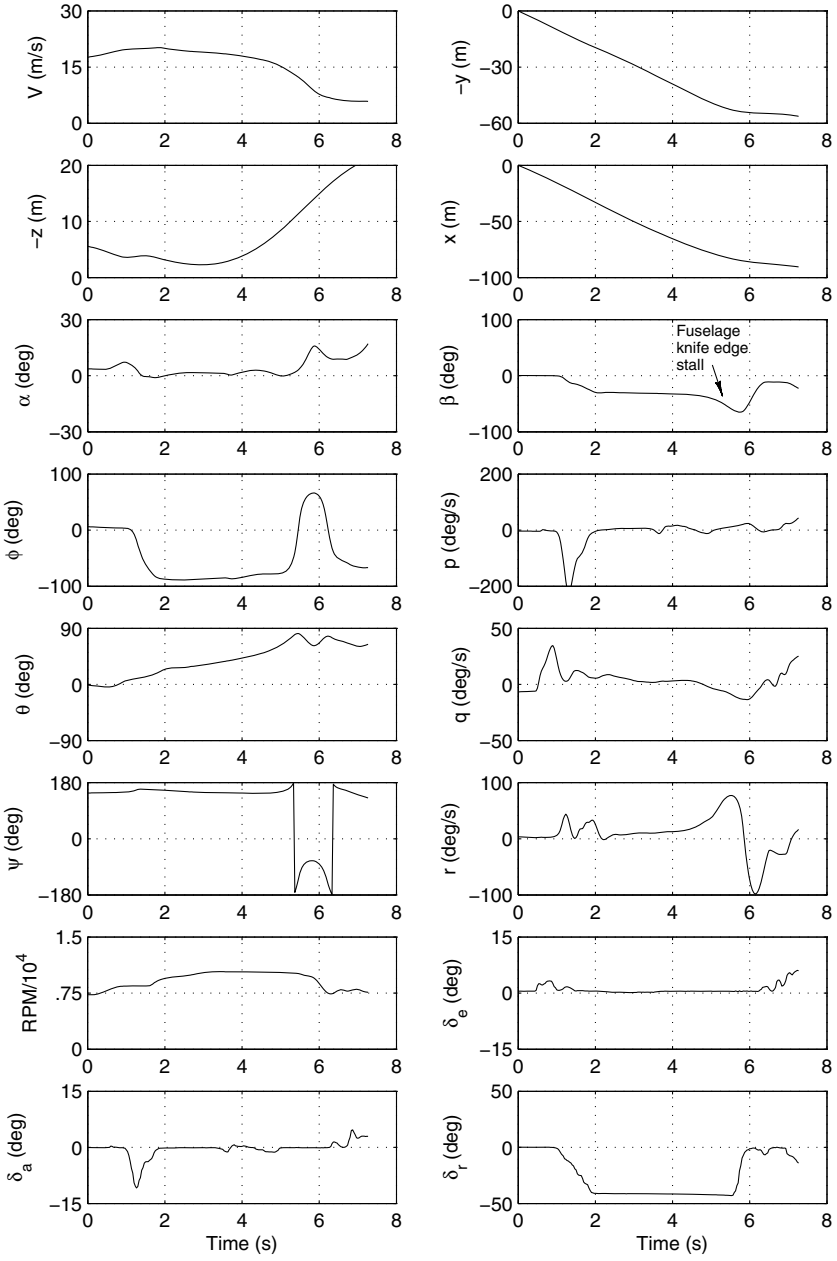

Fig. 21 Time history of the ShowTime 50 aerobatic aircraft in knife-edge flight (see Fig. 20 for trajectory).

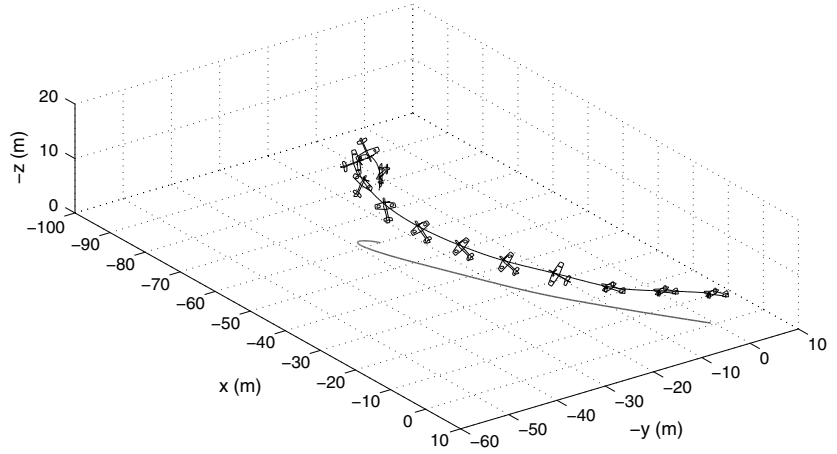

Fig. 22 Trajectory of the ShowTime 50 SFG aerobatic aircraft in knife-edge flight with same input as that use in Fig. 20 [aircraft magnified three times the normal size and drawn every 0.5 s; wingspan of 1448 mm (57 in.)].

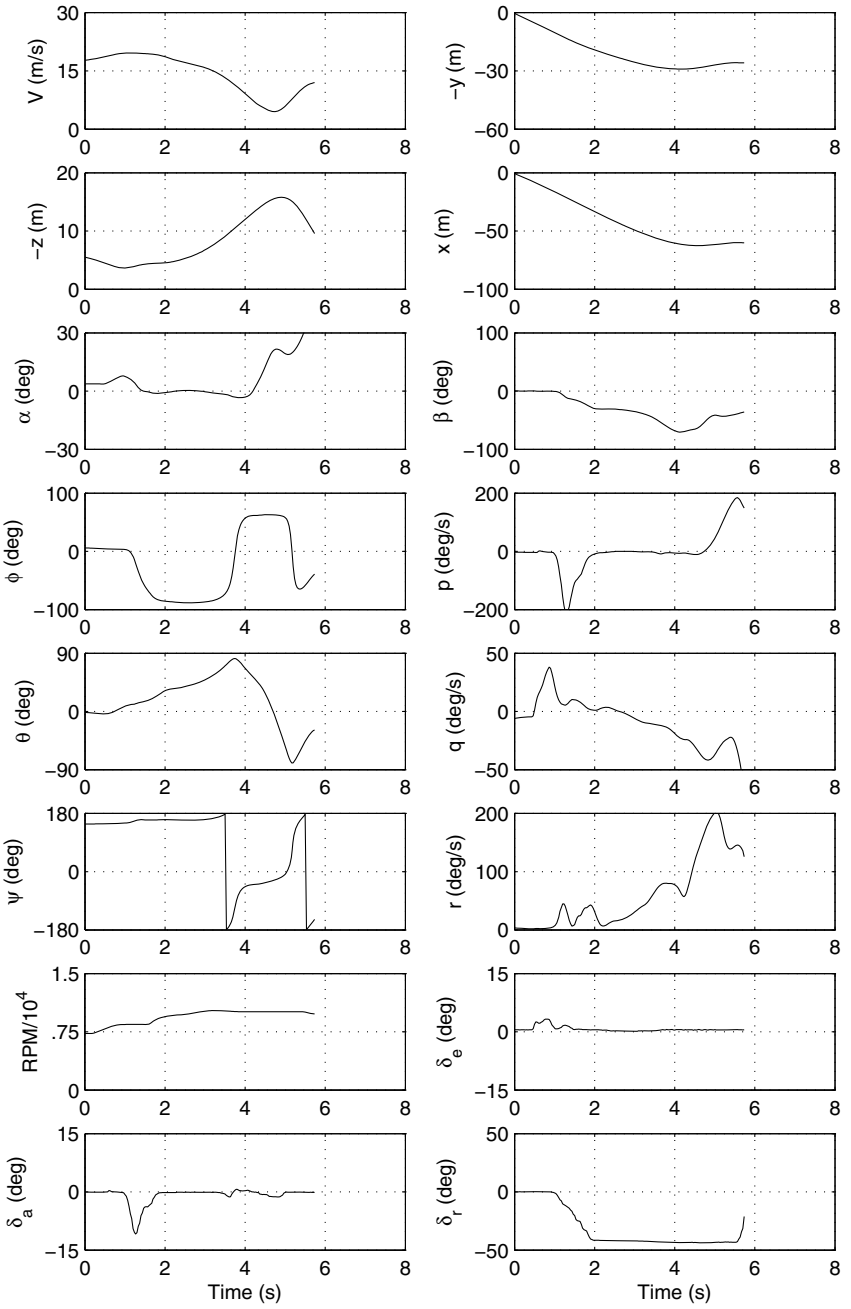

Fig. 23 Time history of the ShowTime 50 SFG aerobatic aircraft in knife-edge flight with same input as that use in Fig. 20 (see Fig. 22 for trajectory).

$$T = \rho n^2 D^4 C_T \tag{23}$$

$$Q = \rho n^2 D^5 C_Q \tag{24}$$

in which the thrust and torque coefficients are determined through lookup tables on the advance ratio given by

$$J = \frac{V_N}{nD} \tag{25}$$

In the method, the propeller thrust and torque coefficients are determined from the blade-element momentum theory, in particular, using the code PROPID [73–75].

Apart from the basic propeller aerodynamics expressed in Eqs. (23) and (24), a number of other factors must be considered for any general motion and propeller attitude. These include propeller normal force and P-factor (yawing moment) when the flow is not axial (i.e., when the propeller is at an angle of attack to the flow). These effects are given by [67] as

$$P_N = \frac{\sigma q A}{2}\left\{\bar{C}_l + \frac{aJ}{2\pi}\ln\left[1+\left(\frac{\pi}{J}\right)^2\right] + \frac{\pi}{J}C_d\right\}\alpha \tag{26}$$

$$N_P = \frac{-\sigma q A R}{2}\left\{\frac{2\pi}{3J}\overline{C}_l + \frac{a}{2}\left[1-\left(\frac{J}{\pi}\right)^2\ln\left(1+\left[\frac{\pi}{J}\right]^2\right)\right] - \frac{\pi}{J}C_d\right\}\alpha \tag{27}$$

in which the average lift coefficient $\bar{C}_l$ is expressed as

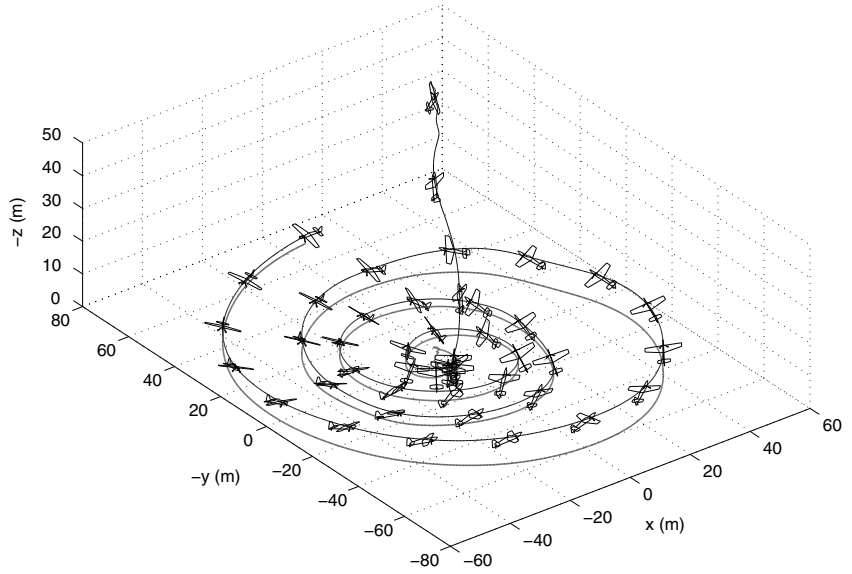

Fig. 24 Trajectory of the 33%-scale Edge 540 aerobatic aircraft in a high-angle-of-attack harrier [aircraft magnified four times the normal size and drawn every 2 s; wingspan of 2476.5 mm (97.5 in.)].

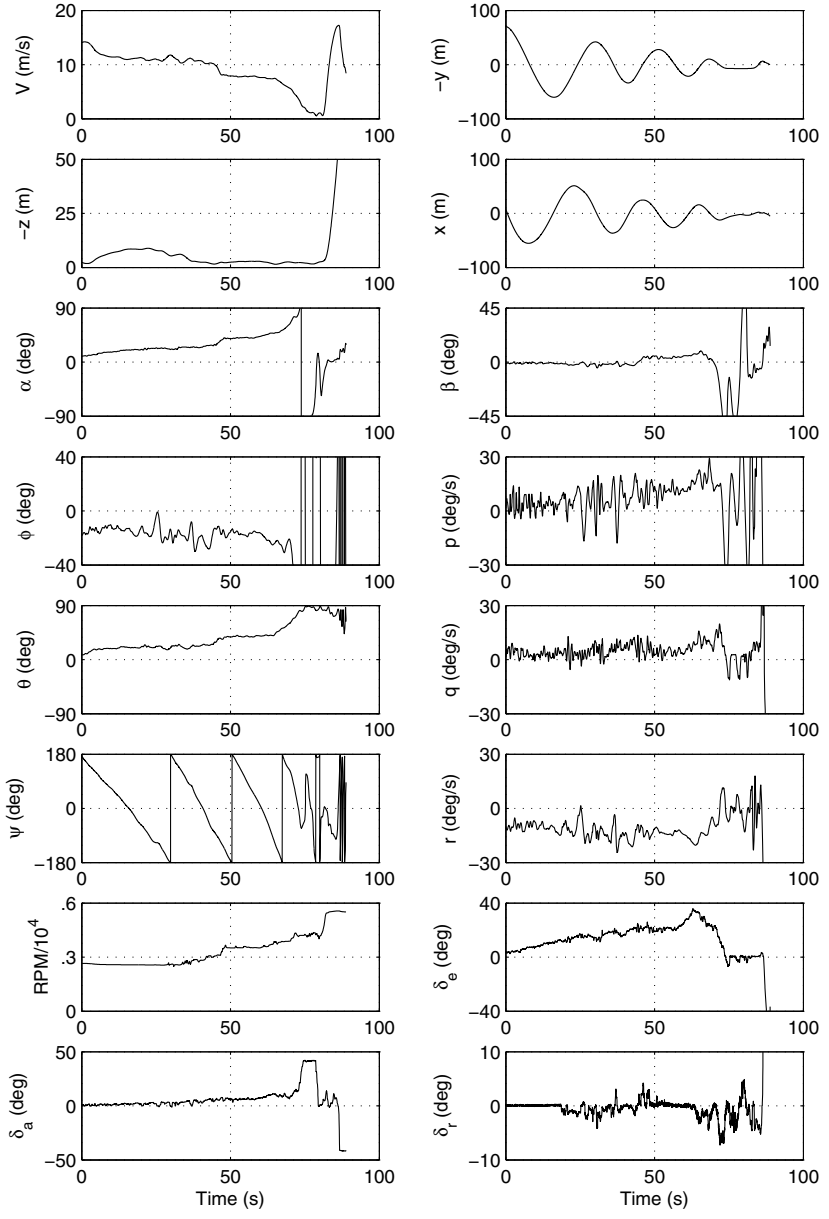

Fig. 25 Time history of the 33%-scale Edge 540 aerobatic aircraft in a high-angle-of-attack harrier (see Fig. 24 for trajectory).

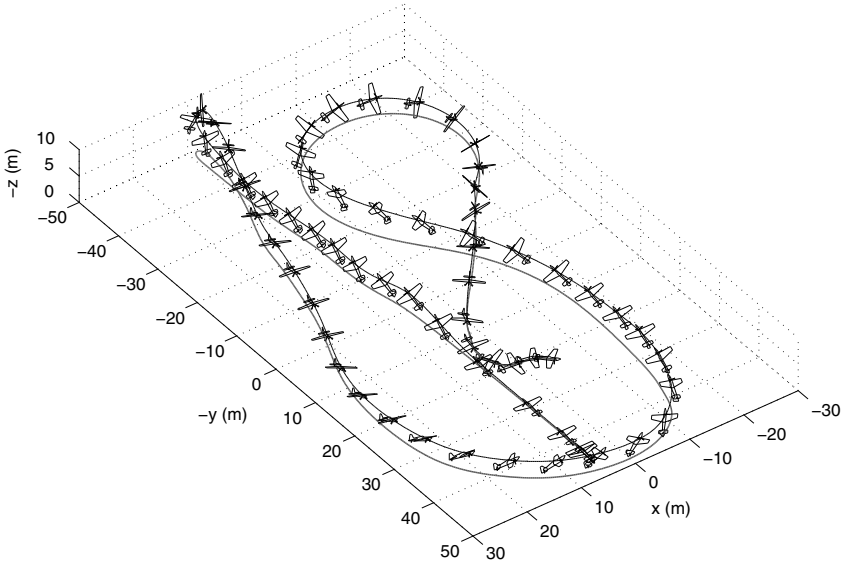

Fig. 26 Trajectory of the 33%-scale Edge 540 aerobatic aircraft in upright and inverted harriers [aircraft magnified two times the normal size and drawn every 0.75 s; wingspan of 2476.5 mm (97.5 in.)].

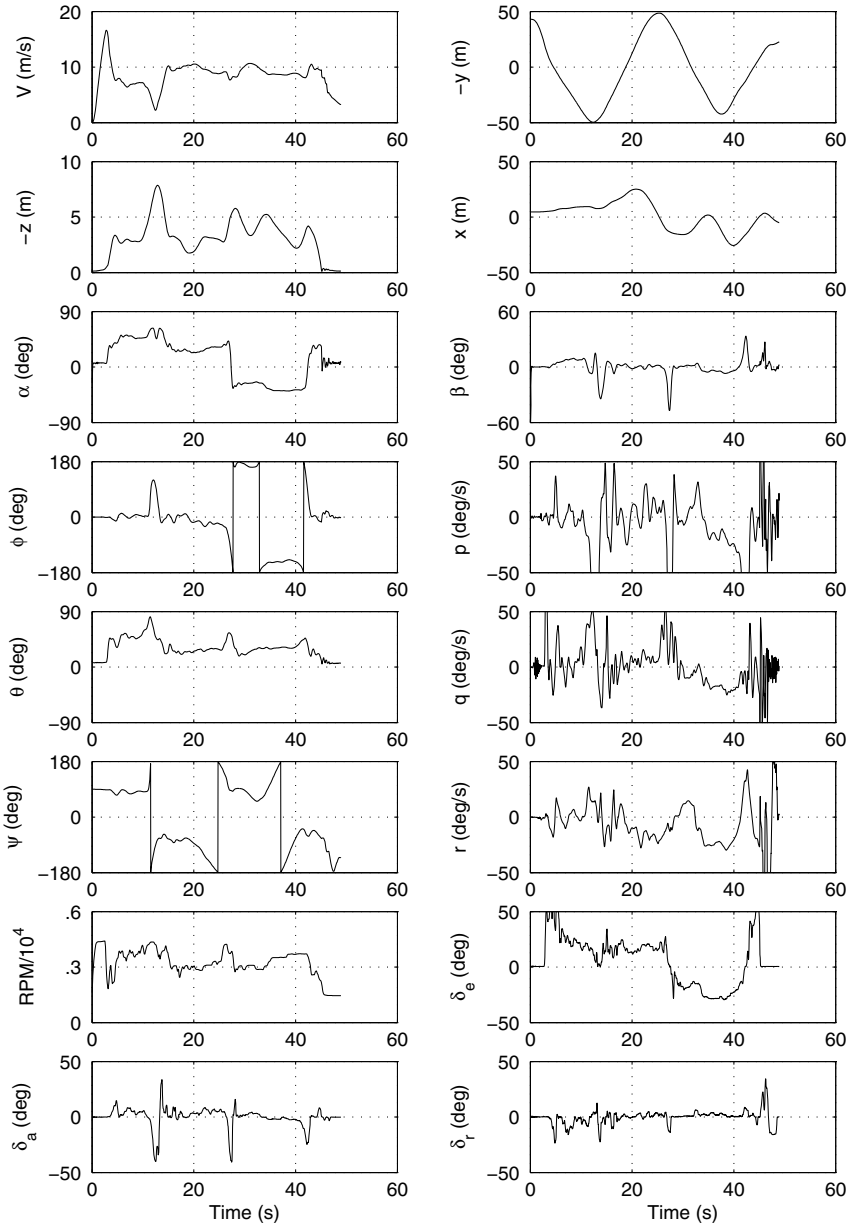

Fig. 27 Time history of the 33%-scale Edge 540 aerobatic aircraft in upright and inverted harriers (see Fig. 26 for trajectory).

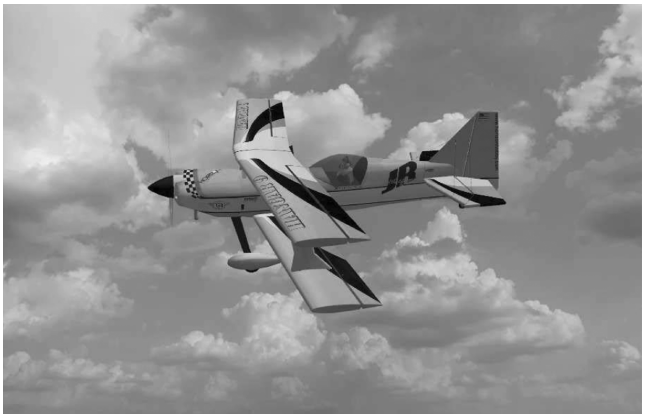

Fig. 28 Ultimate TOC biplane (46% scale) used in simulations [rendering taken from simulator; wingspan of 2540 mm (100 in.)].

$$\bar{C}_l = \left(\frac{3J}{2\pi}\right)\left[\frac{2}{\sigma q A}\frac{J}{\pi}T + C_d\right] \tag{28}$$

in which $C_d = 0.015$ is used during real-time computations. A number of other significant and important propeller effects are modeled [32], such as propeller gyroscopic forces, aerodynamic moments from propeller wake swirl on downstream surfaces (wing, fuselage, and tail), propeller wash/tail-surface damping effects, and propeller-wash lag and wake curvature.

V. Simulation Framework and Validation

The full-envelope aerodynamic modeling methods as described are used in the flight simulator FS One [31], which includes over 30 aircraft that are listed in [76]. The specific aircraft modeled in this paper are shown in Table 1, and the same information in English units is given in Table 2. The simulation solves the full 6-DOF equations of motion using quaternions [77], and integration is carried out using a fourth-order Runge–Kutta scheme capable of running at 300 Hz on a desktop PC. The simulator allows for pilot control input through a standard RC transmitter, from any standard universal-serial-bus joystick, or from a data file.

The code base is written in C++, is object oriented, and includes approximately 600,000 lines of code together with 400,000 lines of code (various languages) for aerodynamic model development. A large number of data files for aerodynamics, graphics, ground terrain-elevation data, textures, etc. are read at run time and make up a substantial part of the overall simulation framework and modeling.

Wind, the atmospheric boundary layer, and turbulence are modeled using a full 3-D turbulent flowfield environment that captures lateral and longitudinal changes along the aircraft extent (wingtip to wingtip, nose to tail). Tabular turbulence data are generated a priori, read at run time, and used in real time to obtain the turbulence quantities for all aircraft components [78,79]. Also, slope winds and wind shear are modeled and used for slope-soaring and dynamic-soaring simulation [80].

The framework described here is the beginning of a new capability for the simulation and modeling of full-envelope aircraft flight dynamics. The validation of the approach relies on the validation of the aerodynamic subsystem component models, which has been accomplished step by step for most components described. However, as with any simulation environment, especially in this case involving full-envelope modeling, elements of the simulation must depend to some extent on tuning of parameters to mimic known flight behaviors. Any tuning must result in prescribed data that remain within reasonable physical bounds, such as the approach used here to model the shielding effects at high angles. Where tuning of physical models is used, any of these methods are candidates for refinement by other means as new data become available, for example, when full aircraft wind-tunnel testing becomes routinely available [9] and/or when it is economical to simulate in CFD defined spin states that could be used to advance models for use in real-time simulations. Finally, in the development of the approach, field tests were performed, recorded on video, and used in tuning and refining the methods. Moreover, every airplane in the simulator, and hence, its underlying models, was tested by professional RC pilots (many having more than 30 years of experience in flying RC models at all levels). The comments by the pilots were, in sum, that the simulation was highly realistic across the broad range of aircraft simulated.

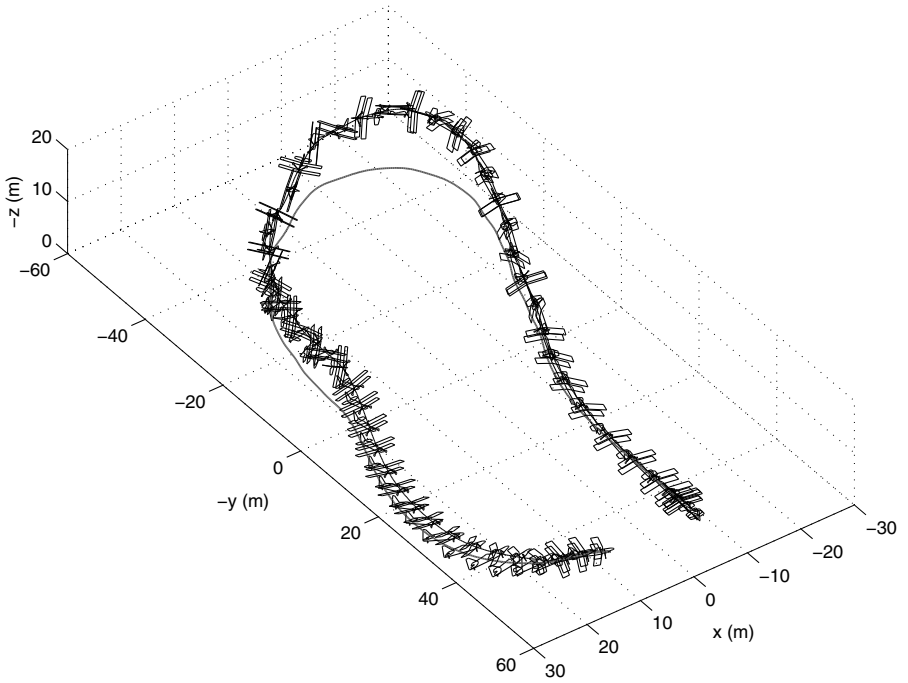

Fig. 29 Trajectory of the 46%-scale Ultimate TOC aerobatic aircraft performing rolling harriers [aircraft magnified 2.5 times the normal size and drawn every 0.45 s; wingspan of 2540 mm (100 in.)].

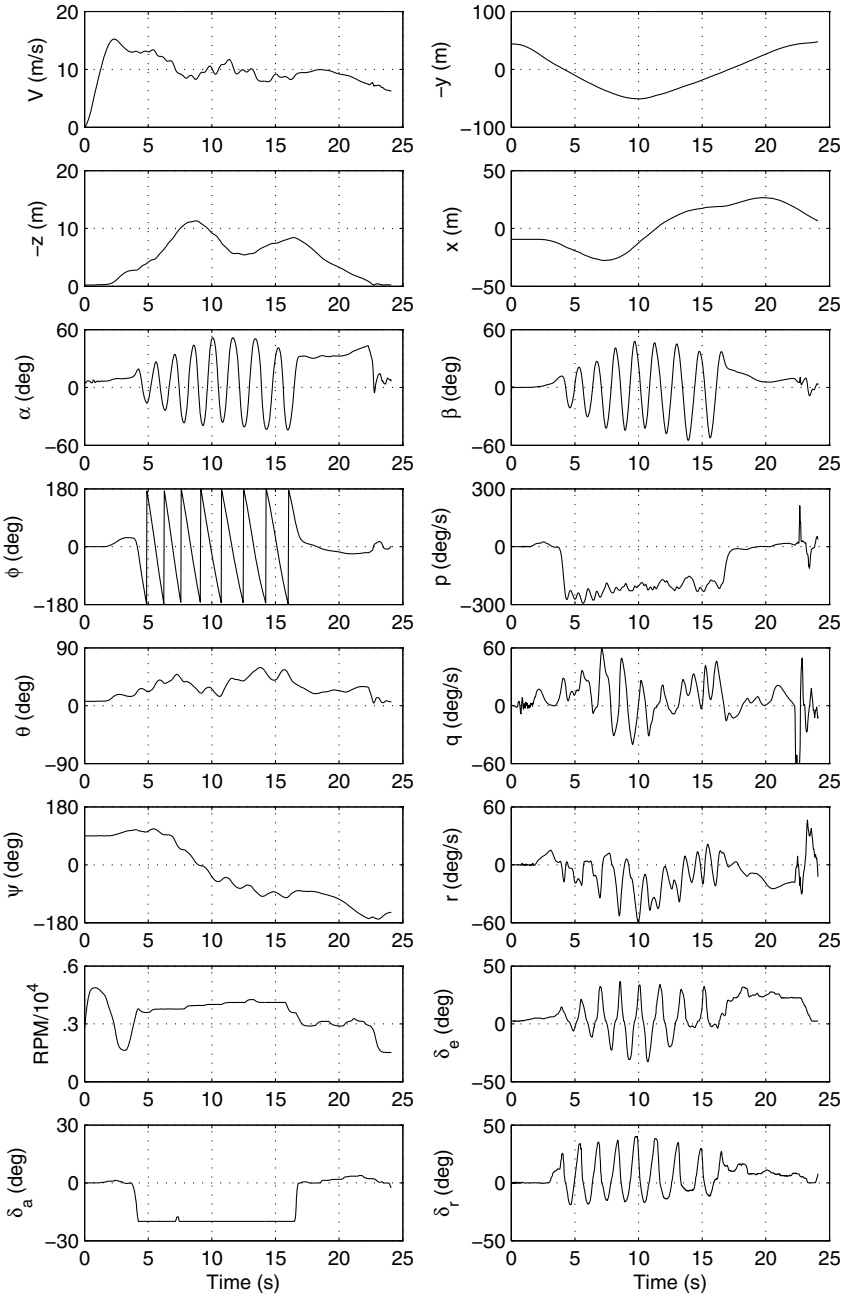

Fig. 30 Time history of the 46%-scale Ultimate TOC aerobatic aircraft performing rolling harriers (see Fig. 29 for trajectory).

VI. Simulations and Discussion

In this section, the flight-simulation results of four airplanes performing aerobatic-type maneuvers are discussed. The maneuvers are briefly described using the flight-path trajectory and aircraft-state-data time histories. Superimposed on the trajectory is a skeleton outline of the aircraft oriented accordingly, and the ground trace is also shown. Although the flight dynamics is carried out at 300 Hz, the time-history data are plotted at a rate of 30 Hz. For several of the flights described, the maneuver is complex and difficult to ascertain based on these short descriptions and graphics alone. In these cases, videos of these flights can be viewed online.[†] All of the flights presented here were performed by the author, and the results are consistent with observations of the real aircraft.

[†]All simulated flights were recorded as videos and are available online at http://aerospace.illinois.edu/m-selig/animations [accessed 3 September 2010].

A. Tailslide

The first simulation is a tailslide of the Extra 260 (configuration shown in Fig. 1) in longitudinal flight with no control inputs used, and the propeller is static for the duration of the flight. The initial aircraft pitch angle θ is 92 deg, the angle of attack is -178 deg, and the aircraft begins at rest. Figure 16 shows the resulting trajectory in the y-z plane, and Fig. 17 shows the corresponding time history. As noted in the figure caption, the aircraft is rendered at 2.5 times the normal size, and it is drawn every 0.55 s in this particular case. As the airplane begins to slide, it is statically unstable in this direction of flight, and thus, the nose begins to pitch toward the ground (positive q). After 1 s, the airplane flips around, nose first. When this happens, the following occur rapidly: pitch rate peaks, airspeed drops, pitch angle passes through -90 deg, and the angle of attack reaches a positive value. Thereafter, the gliding airplane zooms and enters the phugoid mode, in which the angle of attack approaches nearly a constant value before landing at $\approx$7.9 s.

B. Tailslide with Aileron Input

This next case is the same as before, except full left-aileron input (which is opposite that shown in Fig. 1) is used and held constant for the flight. Also, the initial pitch angle is 90 deg. With the flow directly from behind, the initial angle of attack is 180 deg, and as the airplane falls, the flow moves past 180 to −180 deg before flipping around and flying in nose-forward flight. As would be expected, the aircraft in the tailslide first rolls right (positive p) due to reverse flow on the wing, and then after turning around nose first, it rolls left (negative p), as shown in Figs. 18 and 19. When the airplane is released, the initial sideslip angle begins from a value of 180 deg, and this value is used in the aerodynamic calculations. The time history, however, does not show this because the angle plotted is taken from the aircraft state, in which it is defined per convention to be $\beta = \arcsin(v/V)$, which is always limited to ±90 deg.

C. Knife-Edge Flight

The ShowTime 50 aircraft can be configured with or without wing SFGs (configuration shown in Fig. 3). With the SFGs, knife-edge flight is enhanced, and this increased performance can be shown in simulation. Figures 20 and 21 are for the ShowTime 50 without SFGs entering a roll and thereafter sustaining knife-edge flight with largely right-rudder input. The rudder input is held constant until eventually the fuselage stalls in knife-edge flight, reaching a sideslip angle of near −65 deg, and rudder input is relieved near 5.5 s. These same inputs (although truncated in time) were used for the configuration with SFGs, and the results are shown in Figs. 22 and 23. With SFGs, the aircraft climbs in knife-edge flight, and initiates a knife-edge loop.

D. High-Angle-of-Attack Flight: Harrier

With thrust-to-weight ratios of 2 : 1, slow flight under power at high angle of attack in the poststall regime is possible. In model aviation, this aerobatic maneuver is called a harrier. Figures 24 and 25 show a long quasi-steady flight that circles tighter and tighter to a center point where the horizontal speed is ultimately arrested, terminating in a vertical exit at the center of the spiral. The aircraft is the 33%-scale Edge 540 listed in Table 1 and sketched in Fig. 2.

The flight begins in normal cruise with the angle of attack near 10 deg. As time goes on, the up-elevator input is continuously increased. At around 30 s into the flight, the throttle is advanced because the airplane passes from normal flight into the high-drag poststall regime (around an angle of attack of 20 deg). Advancing throttle is required to maintain a height just above ground level. As the flight continues, the up-elevator input is increased, the pitch angle increases, the flight speed slows, and the throttle is advanced to counter the increase in drag and loss in wing lift. The resulting slow flight and high pitch are the distinctive hallmarks of a harrier maneuver. This result can be seen in the trajectory where the pitch increases and the airplane slows (shorter spacing between aircraft plotted at a time interval of 2 s). At the center of the spiral, the airplane is ultimately slowed to a hover position, and pointed straight up before advancing the throttle and climbing out (increasing $-z$).

E. Upright and Inverted Harrier Sequence

Harriers can be performed upright or inverted, and Figs. 26 and 27 show a flight that includes both for the Edge 540. Apart from the climbing roll at 12 s (at $-y \approx -50$ m in Fig. 26), the aircraft is upright until approximately 27 s into the flight (at $-y \approx 50$ m) when the airplane rolls inverted. The transition can be seen in the angle of attack going from positive to negative, and the elevator deflection changing from up elevator to down elevator, which maintains the harrier high angle of attack. Worth noting are the accelerations (changes) in roll, pitch, and yaw rates. When upright for the first ≈27 s, the aircraft is more unsteady and difficult to fly, whereas when inverted, the excursions are reduced. In real observations, upright harrier flights of model-scale aircraft are known to wing rock [41], and this characteristic is partly captured by the simulation as demonstrated here in the time histories.

F. Rolling Harriers

As it sounds, rolling harriers involve rolling flight at slow speeds while maintaining a high pitch angle. The roll is achieved with constant aileron deflection, while the high pitch angle is supported by modulating the elevator and rudder input out of phase once per roll. As an example, for a left roll, up elevator is used when upright, followed by right rudder when in knife edge. As the roll continues into an inverted attitude, down elevator is used, followed by left rudder when in knife edge. The cycle continues for each harrier roll.

Rolling harriers were simulated using the 46%-scale Ultimate TOC biplane shown in Fig. 28 (see Table 1). Figures 29 and 30 show the rolling-harrier maneuver. After takeoff, a left roll begins at 4 s and ends at 17 s, as seen in the time history of the roll rate p. During this period of time, the aileron input is held constant (full aileron stick input) to maintain the continuous roll. The high pitch angle is apparent in the time histories of the angle of attack and sideslip. These angles modulate out of phase because, for the

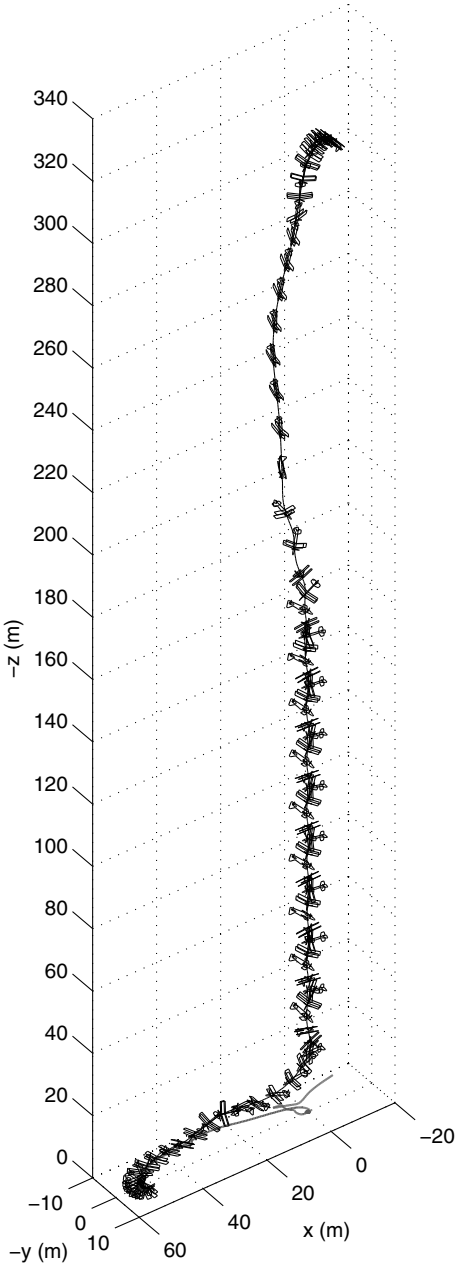

Fig. 31 Trajectory of the 46%-scale Ultimate TOC aerobatic aircraft performing a blender/inverted spin [aircraft magnified 2.5 times the normal size and drawn every 0.365 s; wingspan of 2540 mm (100 in.)].

most part, the roll is axial with positive pitch θ. To sustain the high angle, the elevator and rudder are modulated out of phase, as seen in their time histories. During the turning part of the trajectory near 10 s into the flight, the elevator and rudder inputs are modulated not only out of phase, but also biased to the roll angle so that the airplane is turned by their inputs. Of course, this is difficult to see from the time histories, but in video animation, the effect is clearly visible. One subtle effect are the slight undulations in the elevation z during the roll. These undulations are caused by the aircraft falling through the knife-edge phases of flight while climbing up during wings-level phases of the roll. Some skilled aerobatic pilots notice this effect and synchronize throttle burst inputs with the knife-edge phases to climb at those points, and hence, maintain a more constant elevation, and thus, a more perfect maneuver for visual effect. Finally, it is interesting to see the total harrier angle (angle of attack and sideslip) start small, grow, and then decay. This result is a function of the total net pilot input (elevator and rudder) that is producing the motion.

G. Inverted Spin: The Blender

This last example exercises the edges of the aerobatic envelope — the inverted spin. In particular, the entire vertical maneuver from start to finish is called the blender, shown in Figs. 31 and 32. From a high altitude (≈340 m), the Ultimate TOC biplane begins a dive and accelerates along the vertical line at near 90 deg pitch angle θ. At 5.7 s into the flight, a left-aileron pulse input produces a rapid roll rate p. A fraction of a second after this point, at 6.2 s, rapid down-elevator and right-rudder inputs cause the airplane to pitch inverted (negative q, increasing θ) and yaw. At this point, the energy in the angular momentum that was focused around the roll axis (x) is transferred to angular momentum around the yaw axis (z). In the process, the total angular momentum is more or less conserved. At just the point where the transition begins (starts at 6.2 s), the visual effect is dramatic, with the airplane yaw rate peaking and the pitch attitude flattening. Starting at 6.7 s, the aileron input is relieved, while the elevator and rudder inputs are maintained. The airplane then settles into a steady slow-descent inverted spin at idle throttle setting. As the airplane

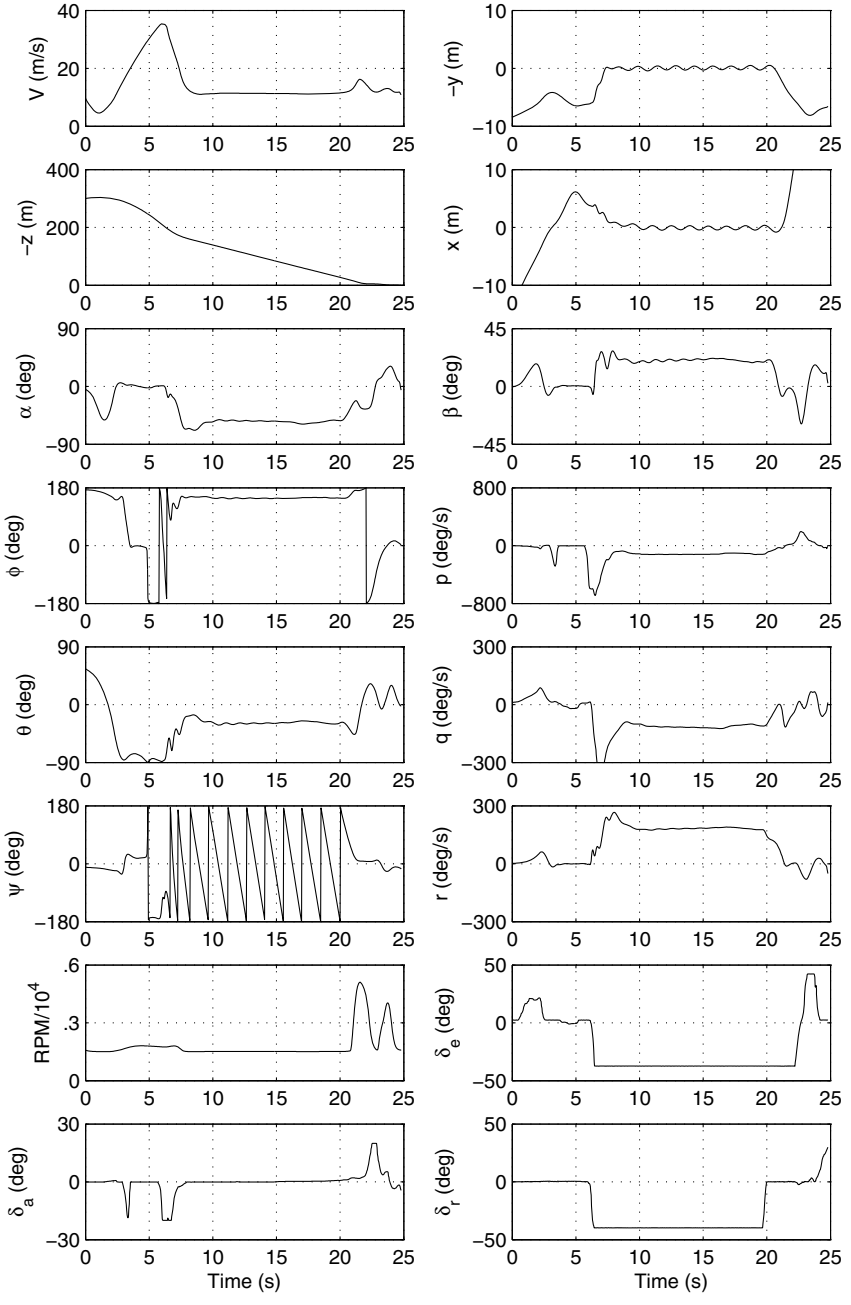

Fig. 32 Time history of the 46%-scale Ultimate TOC aerobatic aircraft performing a blender/inverted spin (see Fig. 31 for trajectory).

Table 3 Roll, pitch, and yaw rates for the Extra 260 EFL and Edge 540 with step control inputs

Deflection, deg	Roll, pitch, and yaw rates, deg /s	Nondimensional roll, pitch, and yaw rates
Extra 260 EFL, $V = 10.2$ m/s		
$\delta_a = -38.8$	$p = -487.8$	$\bar{p} = -0.342$
$\delta_e = -31.7$	$q = 360.1$	$\bar{q} = 0.063$
$\delta_r = 43.9$	$r = -252.6$	$\bar{r} = -0.178$
Edge 540, $V = 27.4$ m/s		
$\delta_a = -39.8$	$p = -490.2$	$\bar{p} = -0.390$
$\delta_e = -42.8$	$q = 261.0$	$\bar{q} = 0.034$
$\delta_r = 39.6$	$r = -163.0$	$\bar{r} = -0.126$

spins, the heading (ψ) changes continuously at a nearly constant rate ($\approx$1.46 s per rotation). The periodicity can also be seen in the trajectory (Fig. 31), in which the interval between aircraft renderings is 0.365 s, or once every 90 deg of spin rotation. Once the steady spin develops, the ground trace is nearly circular (a tiny circle in the figure), and the changes in x and y time histories are thus sinusoidal (see Fig. 32). Termination of the downline spin begins at 20 s where rudder input is released, followed by advancing throttle, then corrective opposite aileron input to roll from inverted to upright (seen in Figs. 31 and 32 near $z = -4.5$ m and $t = 22$ s), and finally nose-up elevator input before flaring to land.

H. Nondimensional Rates

As a point of reference, Table 3 shows the roll, pitch, and yaw rates for the Extra 260 EFL and Edge 540 resulting from step control inputs in aileron, elevator, and rudder, respectively. The initial conditions corresponded to nominally steady-level flight at a typical cruise speed for the respective aircraft. As compared with conventional full-size aircraft, these values illustrate the high maneuverability. For instance, [23] shows that a suitable roll-rate response to aileron for a highly maneuverable fighter or aerobatic airplane is $\bar{p} \geq 0.09$, whereas the values for these aircraft with large aileron authority are much higher. Moreover, in slow, high-angle-of-attack flight when the propeller can provide much of the lift, the flight speed can approach zero, and these nondimensional rates are increased.

VII. Conclusions

This paper shows that complex aerobatic full-envelope maneuvers performed by agile RC/UAV configurations can be simulated using $\pm$180 deg high-angle data in the component-based approach described here. The wings, tail, fuselage, etc. are all modeled separately with corrections applied for any interactions. To capture wide excursions that can occur along the span of the wing, such as in a spin, each wing is subdivided into sections and modeled individually, taking into account the appropriate downwash effects. It is believed that this strip-theory approach is most likely the best way to capture myriad complex nonlinear aerodynamic effects in real-time fixed-wing aircraft simulations, and the approximation has many avenues for advancement. The tail surfaces are modeled separately (e.g., right horizontal tail, left horizontal tail, etc). However, each tail-surface component is not subdivided using a lifting-line-theory approach, but rather modeled as a full surface. No stability derivatives are used because it is believed that such an approach is not amenable to modeling a $\pm$180 deg high-angle flight. Rather full aerodynamic coefficients (e.g., $C_l, C_d, \ldots, C_L, C_D, \ldots$) are used. A key element of the current approach involves calculating the local relative flow that takes into account all effects — flight speed, kinematics of the aircraft rotation motions, propeller wash, downwash, and any shielding effects of one surface on another. New approaches to predicting local airfoil-section data at high angle with large control-surface deflections are also believed to be a key in the success of the method, but these details are not included in the current paper. This approach in aggregate is able to model challenging problems in aerodynamics and flight dynamics, including aircraft spin, for example, as was shown here — the complex inverted spin of a biplane configuration. While the simulations rely on the validity of subcomponent models that in aggregate are consistent with recorded video observations and pilot experience, the models could be further advanced through flight testing, albeit with its own set of challenges required to faithfully capture high-quality measurements of extreme flight.

Acknowledgments

The author would like to thank Brian W. Fuesz and Chris A. Lyon for programming the framework of the simulator that includes the methods described in this paper. Also, the aircraft design and development group at Horizon Hobby, Champaign, Illinois is gratefully acknowledged for partly supporting the initial development of the simulator. Camille Goudeseune and Boris Sergeev are gratefully acknowledged for their ongoing contributions in source code development. The author wishes to acknowledge Pritam P. Sukumar for his efforts in assisting in preparation of some of the plots included in this paper. Rick Deltenre is thanked for the ShowTime 50 aircraft graphics rendering in Fig. 3. Finally, the author thanks the three anonymous reviewers for their valuable comments and suggestions.

References

[1] Taylor, D. J., Ol, M. V., and Cord, T., "SkyTote: An Unmanned Precision Cargo Delivery System," AIAA Paper 2003-2753, July 2003.

[2] Blauwe, H. D., Bayraktar, S., Feron, E., and Lokumcu, F., "Flight Modeling and Experimental Autonomous Hover Control of a Fixed Wing Mini-UAV at High Angle of Attack," AIAA Paper 2007-6818, Aug. 2007.

[3] Frank, A., McGrew, J. S., Valenti, M., Levine, D., and How, J. P., "Hover, Transition, and Level Flight Control Design for a Single-Propeller Indoor Airplane," AIAA Paper 2007-6318, Aug. 2007.

[4] Sobolic, F. M., and How, J. P., "Nonlinear Agile Control Test Bed for a Fixed-Wing Aircraft in a Constrained Environment," AIAA Paper 2009-1927, April 2009.

[5] Kubo, D., and Suzuki, S., "Tail-Sitter Vertical Takeoff and Landing Unmanned Aerial Vehicle: Transitional Flight Analysis," *Journal of Aircraft*, Vol. 45, No. 1, 2008, pp. 292–297. doi:10.2514/1.30122

[6] Stone, R. H., "Aerodynamic Modeling of the Wing–Propeller Interaction for a Tail-Sitter Unmanned Air Vehicle," *Journal of Aircraft*, Vol. 45, No. 1, 2008, pp. 198–210. doi:10.2514/1.15705

[7] Stone, R. H., "Flight Testing of the T-Wing Tail-Sitter Unmanned Air Vehicle," *Journal of Aircraft*, Vol. 45, No. 2, 2008, pp. 673–685. doi:10.2514/1.32750

[8] Barlow, J. B., Rae, W. H., Jr., and Pope, A., *Low-Speed Wind Tunnel Testing*, 3rd ed., Wiley, New York, 1999, pp. 435–441.

[9] Ol, M., Zeune, C., White, T., and Kudla, T., "Wind Tunnel Evaluation of Powered Static Aerodynamics of an Aerobatic UAV," AIAA Paper 2013-0241, Jan. 2013.

[10] Salas, M. D., "Digital Flight: The Last CFD Aeronautical Grand Challenge," *Journal of Scientific Computing*, Vol. 28, No. 2–3, Sept. 2006, pp. 479–505. doi:10.1007/s10915-006-9087-7

[11] Mavriplis, D. J., Darmofal, D., Keyes, D., and Turner, M., "Petaflops Opportunities for the NASA Fundamental Aeronautics Program," AIAA Paper 2007-4084, June 2007.

[12] Tomac, M., and Rizzi, A., "Creation of Aerodynamic Database for the X-31," AIAA Paper 2010-0501, Jan. 2010.

[13] Ghoreyshi, M., Badcock, K. J., and Woodgate, M. A., "Accelerating the Numerical Generation of Aerodynamic Models for Flight Simulation," *Journal of Aircraft*, Vol. 46, No. 3, May–June 2010, pp. 972–980. doi:10.2514/1.3962610.2514/1.39626

[14] Klein, V., and Morelli, E. A., *Aircraft System Identification: Theory and Practice*, AIAA Education Series, AIAA, Reston, VA, 2006.

[15] Jategaonkar, R. V., "A Time Domain Methodology," *Flight Vehicle System Identification*, edited by Lu, F. K., Vol. 216, *Progress in Astronautics and Aeronautics*, AIAA, Reston, VA, 2006.

[16] Petrilli, J., Paul, R., Gopalarathnam, A., and Frink, N. T., "A CFD Database for Airfoils and Wings at Post-Stall Angles of Attack," AIAA Paper 2013-2916, June 2013.

[17] Finck, R. D., "USAF Stability and Control DATCOM," U.S. Air Force Wright Aeronautical Lab., AFWAL, TR-83-3048, Wright–Patterson AFB, OH, Oct. 1960 (rev. 1978).
[18] "ESDU Data Sheets," IHS ESDU, London, http://www.esdu.com/ [retrieved 5 Nov. 2013].
[19] Tobing, S., Go, T. H., and Vasilescu, R., "Improved Component Buildup Method for Fast Prediction of the Aerodynamic Performances of a Vertical Takeoff and Landing Micro Air Vehicle," *Computational Fluid Dynamics 2008*, Springer, Berlin/Heidelberg, 2009, pp. 209–214.
[20] Guerrero, I., Londenberg, K., Gelhausen, P., and Myklebust, A., "A Powered Lift Aerodynamic Analysis for the Design of Ducted Fan UAVs," AIAA Paper 2003-6567, Sept. 2003.
[21] Evans, J., and Nahon, M., "Dynamics Modeling and Performance Evaluation of an Autonomous Underwater Vehicle," *Ocean Engineering*, Vol. 31, Nos. 14–15, 2004, pp. 1835–1858. doi:10.1016/j.oceaneng.2004.02.006
[22] Saephan, S., and van Dam, C. P., "Determination of Wing-Only Aircraft Tumbling Characteristics Through Computational Fluid Dynamics," *Journal of Aircraft*, Vol. 45, No. 3, May–June 2008, pp. 1044–1053. doi:10.2514/1.33730
[23] Phillips, W. F., *Mechanics of Flight*, 2nd ed., Wiley, New York, 2010, pp. 661–666.
[24] Paul, R., and Gopalarathnam, A., "Simulation of Flight Dynamics with an Improved Post-Stall Aerodynamics Model," AIAA Paper 2012-4956, Aug. 2012.
[25] Dickes, E. G., and Ralston, J. N., "Application of Large-Angle Data for Flight Simulation," AIAA Paper 2000-4584, Aug. 2000.
[26] Foster, J. V., Cunningham, K., Fremaux, C. M., Shah, G. H., Stewart, E. C., Rivers, R. A., Wilborn, J. E., and Gato, W., "Dynamics Modeling and Simulation of Large Transport Airplanes in Upset Conditions," AIAA Paper 2005-5933, Aug. 2005.
[27] Gingras, D. R., and Ralston, J. N., "Aerodynamics Modeling for Upset Training," AIAA Paper 2008-6870, Aug. 2008.
[28] Keller, J. D., McKillip, R. M., Jr., and Wachspress, D. A., "Physical Modeling of Aircraft Upsets for Real-Time Simulation Applications," AIAA Paper 2008-6205, Aug. 2008.
[29] Keller, J. D., McKillip, R. M., Jr., and Kim, S., "Aircraft Flight Envelope Determination Using Upset Detection and Physical Modeling Methods," AIAA Paper 2009-6259, Aug. 2009.
[30] Imbrie, A. P., "A Geometrical Study of the Steady-State Spin for a Typical Low-Wing General Aviation Aircraft," *Journal of Aircraft*, Vol. 18, No. 6, June 1981, pp. 510–512.
[31] "FS One, Precision RC Flight Simulator," Software, Ver. 2, InertiaSoft, Champaign, IL, 2014.
[32] Selig, M. S., "Modeling Propeller Aerodynamics and Slipstream Effects on Small UAVs in Realtime," AIAA Paper 2010-7938, Aug. 2010.
[33] Uhlig, D. V., Selig, M. S., and Neogi, N., "Health Monitoring via Neural Networks," AIAA Paper 2010-3419, April 2010.
[34] Wright, J. R., and Cooper, J. E., *Introduction to Aircraft Aeroelasticity and Loads*, Aerospace Series, Wiley, West Sussex, England, 2007, p. 79.
[35] Johnson, W., *Helicopter Theory*, Dover, New York, 1980, pp. 45–51.
[36] McMillan, O. J., Schwind, R. G., Nielsen, J. N., and Dillenius, M. F. E., "Rolling Moments in a Trailing Vortex Flow Field," Nielsen Engineering and Research, NEAR TR-129, Mountain View, CA; also NASA CR-151961, Feb. 1977.
[37] Poppen, A. P., Jr., "A Method for Estimating the Rolling Moment due to Spin Rate for Arbitrary Planform Wings," NASA TM-86365, Jan. 1985.
[38] Pamadi, B. N., and Taylor, L. W., Jr, "Estimation of Aerodynamic Forces and Moments on a Steadily Spinning Airplane," *Journal of Aircraft*, Vol. 21, No. 12, 1984, pp. 943–954. doi:10.2514/3.45067
[39] Pamadi, B. N., *Performance, Stability, Dynamics, and Control of Airplanes*, AIAA Education Series, AIAA, Reston, VA, 1998, pp. 262–270.
[40] X-Plane Flight Simulator, Software, Ver. 9, http://www.x-plane.com [accessed 3 Sept. 2010].
[41] Johnson, B., and Lind, R., "Characterizing Wing Rock with Variations in Size and Configuration of Vertical Tail," *Journal of Aircraft*, Vol. 47, No. 2, March–April 2010, pp. 567–576. doi:10.2514/1.45719
[42] Drela, M., "XFOIL: An Analysis and Design System for Low Reynolds Number Airfoils," *Low Reynolds Number Aerodynamics*, edited by Mueller, T. J., Vol. 54, Lecture Notes in Engineering, Springer–Verlag, New York, June 1989, pp. 1–12.
[43] Sheldahl, R. E., and Klimas, P. C., "Aerodynamic Characteristics of Seven Airfoil Sections Through 180-Degree of Attack for Use in Aerodynamic Analysis of Vertical Axis Wind Turbines," Sandia National Lab., SAND80-2114, Albuquerque, NM, 1981.
[44] Wick, B. H., "Study of the Subsonic Forces and Moments on an Inclined Plate of Infinite Span," NACA TN-3221, 1954.
[45] Ostowari, C., and Naik, D., "Post-Stall Wind Tunnel Data for NACA 44XX Series Airfoil Sections," SERI/STR 217-2559, Jan. 1985.
[46] Sørensen, N. N., Johansen, J., and Conway, S., "CFD Computations of Wind Turbine Blade Loads During Standstill Operation KNOW-BLADE," Risø National Lab., Task 3.1 Rept. Risø-R-1465(EN), Roskilde, Denmark, June 2004.
[47] van Rooij, R. P. J. O. M., "Analysis of the Flow Characteristics of Two Nonrotating Rotor Blades," *Journal of Solar Energy Engineering*, Vol. 130, No. 3, Aug. 2008, Paper 031015. doi:10.1115/1.2931507
[48] Sørensen, N. N., and Michelsen, J. A., "Drag Prediction for Blades at High Angle of Attack Using CFD," *Journal of Solar Energy Engineering*, Vol. 126, No. 4, Nov. 2004, pp. 1011–1016. doi:10.1115/1.1807854.
[49] Spera, D. A., "Models of Lift and Drag Coefficients of Stalled and Unstalled Airfoils in Wind Turbines and Wind Tunnels," NASA CR-2008-215434, Oct. 2008.
[50] Lindenburg, C., "Stall Coefficients," Energy Research Center of The Netherlands ECN-RX-01-004, Petten, The Netherlands, Jan. 2001; also *IEA Symposium on the Aerodynamics of Wind Turbines*, National Renewable Energy Lab., Golden, CO, Dec. 2000.
[51] Tangler, J. L., and Ostowari, C., "Horizontal Axis Wind Turbine Post Stall Airfoil Characteristics Synthesization," edited by Spera, D., Collected Papers in Wind Turbine Technology, DOE/NASA/5776-2, NASA CR-195432, May 1995, pp. 35–39.
[52] Montgomerie, B., "Methods for Root Effects, Tip Effects and Extending the Angle of Attack Range to 180 Deg, with Application to Aerodynamics for Blades on Wind Turbines and Propellers," Swedish Defence Research Agency, FOI-R-1305-SE, Stockholm, Sweden, ISSN 1650-1942, June 2004.
[53] Ericsson, L. E., "Vortex Characteristics of Pitching Double-Delta Wings," *Journal of Aircraft*, Vol. 36, No. 2, March–April 1999, pp. 349–356. doi:10.2514/2.2464
[54] Leishman, J. G., *Principles of Helicopter Aerodynamics*, Cambridge Aerospace Series, Cambridge Univ. Press, Cambridge, England, U.K., 2000, pp. 307–309.
[55] Zimmerman, C. H., "Characteristics of Clark Y Airfoils of Small Aspect Ratios," NACA TR-431, 1933.
[56] Zimmerman, C. H., "Aerodynamic Characteristics of Several Airfoils of Low Aspect Ratio," NACA TN-539, 1935.
[57] Silverstein, A., and Katzoff, S., "Aerodynamic Characteristics of Horizontal Tail Surfaces," NACA TR-688, 1940.
[58] Bates, W. R., "Collection and Analysis of Wind-Tunnel Data on the Characteristics of Isolated Tail Surfaces with and Without End Plates," NACA TN-1291, 1947.
[59] Whicker, L. F., and Fehlner, L. F., "Free-Stream Characteristics of a Family of Low-Aspect-Ratio, All-Movable Control Surfaces for Application to Ship Design," David Taylor Model Basin, Rept. 933, Washington, D.C., Dec. 1958.
[60] Koenig, D. G., "Low-Speed Tests of Semispan-Wing Models at Angles of Attack from 0 to 180," NASA TM-2-27-59A, April 1959.
[61] Kerwin, J. W., Mandel, P., and Lewis, S. D., "An Experimental Study of a Series of Flapped Rudders," *Journal of Ship Research*, Vol. 16, No. 4, Dec. 1972, pp. 221–239.
[62] Marchaj, C. A., *Sail Performance*, Adlard Coles Nautical, London, 1996, pp. 86, 147–148, 187.
[63] Marchaj, C. A., *Aero-Hydrodynamics of Sailing*, Dodd, Mead and Company, New York, 1979, pp. 443–446.
[64] Torres, G., and Mueller, T., "Low-Aspect-Ratio Wing Aerodynamics at Low Reynolds Numbers," *AIAA Journal*, Vol. 42, No. 5, May 2004, pp. 865–873. doi:10.2514/1.439
[65] Desabrais, K. J., "Aerodynamic Forces on an Airdrop Platform," AIAA Paper 2005-1634, May 2005.
[66] Cosyn, P., and Vierendeels, J., "Numerical Investigation of Low-Aspect-Ratio Wings at Low Reynolds Numbers," *Journal of Aircraft*, Vol. 43, No. 3, May–June 2006, pp. 713–722. doi:10.2514/1.16991
[67] McCormick, B. W., *Aerodynamics, Aeronautics, and Flight Mechanics*, 2nd ed., Wiley, New York, 1995, pp. 291–297.
[68] Schlichting, H., and Truckenbrodt, E., *Aerodynamics of the Airplane*, McGraw–Hill, New York, 1979, p. 450.
[69] Neihouse, A. I., and Lichtenstein, J. H., "Tail-Design Requirements for Satisfactory Spin Recovery," NACA TN-1045, 1946.

[70] Burk, S. M., Jr., Bowman, J. S., Jr., and White, W. L., "Spin-Tunnel Investigation of Spinning Characteristics of Typical Single-Engine General Aviation Designs. I: Low-Wing Model A: Effects of Tail Configurations," NASA TP-1009, 1977.

[71] Bowman, J. S., Jr., Hultberg, R. S., and Martin, C. A., "Measurements of Pressures on the Tail and Aft Fuselage of an Airplane Model During Rotary Motions at Spin Attitudes," NASA TP-2939, 1989.

[72] McCormick, B. W., Zilliac, G. G., and Ballin, M. G., "Wind Tunnel Testing and Analysis Relating to the Spinning of Light Aircraft," AIAA Paper 1984-0058, Jan. 1984.

[73] Hibbs, B., and Radkey, R. L., "Calculating Rotor Performance with the Revised PROP Computer Code," Rockwell International, Wind Energy Research Center, RFP-3508, UC-60, Golden, CO, 1983.

[74] Selig, M. S., and Tangler, J. L., "Development and Application of a Multipoint Inverse Design Method for Horizontal Axis Wind Turbines," *Wind Engineering*, Vol. 19, No. 5, 1995, pp. 91–105.

[75] Selig, M. S., "PROPID: Software for Horizontal-Axis Wind Turbine Design and Analysis," http://aerospace.illinois.edu/m-selig/propid.html [accessed 12 May 2014].

[76] Selig, M. S., "Modeling Full-Envelope Aerodynamics of Small UAVs in Realtime," AIAA Paper 2010-7635, Aug. 2010.

[77] Stengel, R. F., *Flight Dynamics*, Princeton Univ. Press, Princeton, NJ, 2004, p. 184.

[78] Ninham, C. P., Raju, R., and Selig, M. S., "A Real-Time Atmospheric Turbulence Model for Aircraft Flight Simulators," AIAA Paper 1998-0668, Jan. 1998.

[79] Kelly, N. D., and Jonkman, B. J., "Overview of the TurbSim Stochastic Inflow Turbulence Simulator," National Renewable Energy Lab., NREL/SR-500-36971, Golden, CO, 2005.

[80] Sukumar, P. P., and Selig, M. S., "Dynamic Soaring of Sailplanes over Open Fields," *Journal of Aircraft*, Vol. 50, No. 5, 2013, pp. 1420–1430. doi:10.2514/1.C031940